PATTERN RECOGNITION IN THE DETECTION OF TUBERCULOUS MENINGITIS

WARREN HALBERSTADT

SUBMITTED TO THE UNIVERSITY OF CAPE TOWN IN PARTIAL FULFILMENT OF THE REQUIREMENTS FOR THE DEGREE OF MSC IN BIOMEDICAL ENGINEERING

DECLARATION

I, Warren Halberstadt, declare that the work set out in this thesis is essentially my own work and that no part has been submitted for a degree at any academic institution

Signed by candidate

SYNOPSIS

The prevalence of Tuberculous Meningitis (TBM) is increasing in countries affected by HIV such as South Africa. This disease affects mainly the young or the immune-suppressed and can cause death or permanent brain damage. Diagnosis of TBM is difficult due to its non-specific signs and the fact that culturing which is the only absolute method of verifying TBM, takes approximately 4 weeks. The role of computed tomography (CT) in diagnosis and treatment has increased dramatically, especially in countries like South Africa that cannot afford Magnetic Resonance Imaging (MRI) in their public hospitals.

Unfortunately, up till now, radiologists have struggled with non-specific signs of TBM on CT images. Most diagnoses of TBM were achieved by looking for various signs on the scans, with each additional sign relating to TBM increasing the chances of TBM being present.

Recently Dr Savvas Andronikou, radiologist at Red Cross Childrens' Hospital, hypothesized a new sign associated with TBM, namely hyperdensity (increased density) of the tissues in the basal cisterns of the brain. He had found the sign on the CT scans of a large proportion of 40 confirmed TBM patients. These patients' CT's were unfortunately all hardcopy films and there was no way for him to measure the density directly and confirm his findings of higher density.

At this stage Dr Andronikou contacted our department to aid him in proving his hypothesis. The initial part of this research therefore lay in reconstructing the original density values from the hardcopy CT. This was accomplished by scanning the images and using the images' window settings to generate a linear ratio between CT number and pixel intensity. This was applied to each pixel in the image, and so the density or CT numbers for the image was reconstructed. The process ended in verification of Dr Andronikou's theory of hyperdensity and formed the basis of our remaining research.

The detection of the hyperdensity even by experienced radiologists is difficult due to the fact that the human eye can only distinguish approximately 16 grey values, where CT images can contain thousands of different grey values. Subtle differences in density may easily be missed by the human eye, and our research sought to develop a means of using pattern recognition to aid in TBM diagnosis.

After examining the past literature it was clear that little research had been done on using pattern recognition on CT images. Most research had focused on MRI images as they have better image quality. We chose fuzzy clustering as the best form of pattern recognition for our study as it had good clustering results and was fairly fast and easy to implement. Fuzzy logic is a way of mathematically representing uncertainty in real world data. Since CT images contain noise, which essentially is uncertainty, it was ideal for use with a clustering algorithm in order to provide more accurate clustering.

We used a modified fuzzy maximum likelihood estimation (FMLE) algorithm when clustering the brain CT images. This algorithm was first introduced by Gath and Geva (1989) and contained several desirable properties for our application.

The algorithm was unsupervised, meaning that it did not rely on prior information about the images, such as how many clusters to use in segmenting the image.

The FMLE algorithm was applied in two stages. The first application resulted in the images being separated into 3 clusters, corresponding to ventricle, skull and brain tissues. A further application of the algorithm to the brain cluster then resulted in the segmentation of the desired hyperdensity cluster.

The combined algorithm was applied to the scans of 17 positive TBM patients and resulted in hyperdense clusters being segmented for all the images. The algorithm was also applied to 9 normal CT images to act as controls, and the 9 control images showed none of the abnormal hyperdensity associated with the TBM patients.

A sign often associated with TBM is hydrocephalus or increased size of the ventricles in the brain. The ventricle cluster segmented by the FMLE algorithm then enabled us to calculate a ventricle to brain area ratio; that gave an indication as to whether the patient was also suffering from hydrocephalus. This ratio meant that we had two signs associated with TBM and a TBM diagnosis could be made with more confidence.

The final conclusions from this study are that hyperdensity is a sign associated with TBM and can be detected on un-enhanced CT brain scans using our algorithm. Other signs of TBM such as hydrocephalus may also be demonstrated after clustering with our algorithm and therefore the program aids the radiologist in making a positive diagnosis of TBM.

ACKNOWLEDGEMENTS

I would like to thank Dr Savvas Andronikou, for his contribution of expert knowledge to the project and his help has been invaluable. Thanks to Prof Beningfield for help with obtaining a scanner for the images used in the project. I would like to thank my family and friends for their support and advice. Lastly a big thanks to my supervisor Dr Tania Douglas for all the input and help she has given me throughout the project.

TABLE OF CONTENTS

TABLE OF FIGURES

1 INTRODUCTION

TB is a worldwide epidemic that is on the rise in most African countries including South Africa. According to the South African National Tuberculosis Association, 1 South African dies from TB every hour (SANTA, 2004). The reason for this high figure is that the rise in HIV infection in South Africa has lead to an increase in cases of TB as they are highly related diseases. Due to the increase in TB cases and HIV there has also been a rise in complications associated with TB. One of the more serious complications is Tuberculous Meningitis (TBM) in children. The disease can lead to serious brain damage and death and is difficult to diagnose due to many non-specific symptoms. The gold standard in testing relies on culturing of the bacteria, but unfortunately the incubation time is four weeks, which is too long to wait without treatment. computed tomography (CT) to aid in diagnosis is gaining widespread usage, where radiologists examine the scans to find a number of visual indicators, or signs of TBM.

A new sign associated with TBM has been proposed by Dr Savvas Andronikou, who recently completed his Phd thesis on TBM and has also published a paper on this subject (Andronikou *et al*, 2004). The sign is hyperdensity in the basal areas of the brain in pre-contrast (or un-enhanced) brain CT scans. In the past, in order for the radiologist to see enhancement of the basal areas, contrast medium was injected into the patients' bloodstream. What this does is increase the contrast in the CT image and makes the differences in density easier to visualise. However, this in an invasive procedure, and adds both risk and expense to the CT scan.

In order to prove this finding of hyperdensity, we needed to verify the hyperdensity from hardcopy CT films of patients who have confirmed TBM. This involved reconstruction of the CT numbers from the digitized films.

Detection of the hyperdensity sign is difficult even for radiologists who are experienced in dealing with TBM. The human eye is unable to detect small differences in density on CT films, and therefore the hyperdensity can easily be missed. We therefore required a method using pattern recognition in order to highlight the hyperdensity that might indicate the presence of TBM.

The ultimate objective of this project was the detection of TBM from CT scans in order to aid the radiologists in their diagnosis. To overcome the problem of detecting hyperdensity with poor contrast, we required a pattern recognition algorithm that was able to distinguish and extract different densities from CT images. A number of other signs are associated with TBM and we therefore hoped to use the same algorithm to extract certain of these signs, which would further aid the radiologist. Lastly we aimed to verify our results by using expert opinion and control data.

The scope of this project was limited to children in the Western Cape region, that were admitted to the Red Cross Children's Hospital with possible TBM, over a period of 4 years (1998-2002). We included 17 positively identified TBM patients and 9 normal (control) patients of the same age group. The long scanning time and logistics involved in scanning the images, eg: access time to the scanner also contributed to the low number of available scans.

The algorithm was programmed in Matlab 6, on a Pentium 4 computer with a 2.4Ghz processor and 512Mb of RAM. Matlab 6 was chosen to write the algorithm, due to its built in functions and ease of use. Although Matlab contains its own fuzzy clustering functions, these were not used in this project. Nearly all the code was written from scratch, for better manipulation and understanding. The programs used in the project are listed in appendix D, which gives a brief overview of what each program does.

Chapter 2 is a review of the relevant literature related to this project. In Chapter 3 the reconstruction of the CT numbers from the hardcopy films is discussed and the results of the reconstruction algorithm are given. Chapter 4 details Fuzzy Clustering and discusses the need for fuzzy logic, as well as detailing several fuzzy algorithms that were utilised in the project. The application of the algorithm to ct scans of TBM patients and the resultant hyperdensity results are discussed in chapter 5. Chapter 6 details the application of the same algorithm to isolate the ventricles in the images, and the subsequent detection of Hydrocephalus as a sign associated with TBM. Conclusions and discussion of the outcome of the project are found in chapter 7, while the appendices and references are found in chapters 8 and 9 respectively.

2 LITERATURE REVIEW

2.1 Tuberculous meningitis (TBM)

According to the Merck manual of clinical diagnosis (1992), tuberculous meningitis is one of the most dreaded complications of TB and is the spread of TB into the subarachnoid space at the base of the brain often causing severe neurological defects.

Tuberculosis is one of South Africa's largest epidemics, outstripped at the moment by HIV aids. According to the South African Department of Health, the incidence of Tuberculosis in 2001 was 496 cases per 100 000 people and 49% of South African TB sufferers have HIV/AIDS (South African Department of Health Statistics, 2004). TBM has been identified as a potential complication of HIV infection, and the risk of developing TBM is vastly increased with the presence of Aids (Bishburg *et al*, 1986). The high level of TB and HIV infection in children has lead to an increased number of cases of TBM in South African hospitals.

In places where TB is common among children (South Africa for example) tuberculous meningitis usually occurs between ages 1 and 5. Symptoms are fever, headache, nausea, drowsiness leading to stupor and coma as the illness progresses. The illness is categorized into stages, with varying symptoms for each stage, and each progressive stage is associated with an increase in the likelihood of CNS defects becoming permanent.

Symptoms and signs of TBM described in the literature do not seem to be consistent from one study to the next. For example a symptom such as Fever is found to have wide variation ranging from 13% to 65% of TBM cases (Thwaites *et al,* 2000). The lack of definitive symptoms has lead to a number of tests being proposed in order to improve diagnosis.

Examination of the cerebro-spinal fluid (CSF) is a common diagnostic tool used for TBM. A lumbar puncture test is performed where the CSF is removed from the spinal cord. The CSF is tested for raised protein levels and reduced glucose levels. Although these tests aren't conclusive, they do aid in the diagnosis.

By using Ziehl- Neelson staining on a CSF sample, the laboratory attempts to find acid fast bacilli in the CSF, another indicator of TBM, but once again not conclusive. The sensitivity of the test in the literature ranges from 10% to 87% (Thwaites *et al,* 2000).

Newer methods of diagnosis, such as using amplification of bacterial DNA are proving successful. Unfortunately they have not been completely assessed and are too expensive to run in developing countries. Another new test includes the tuberculostearic acid deformation test, but this can only be performed at specialized laboratories and so again cannot be utilized in this country. The gold standard of TBM testing is still the culturing of the TB bacteria itself from the CSF. The problem associated with culturing is the long incubation time of approximately 4 weeks. This is unacceptable for cases of TBM as it is well documented that the longer the diagnosis takes, the poorer the prognosis (Thwaites *et al,* 2000).

TBM is formed when the TB bacilli infiltrates the central nervous system and forms a lesion. The rupturing of this lesion is thought to be the cause of the TBM reaction, where the meninges have an acute inflammatory response. A basal meningeal exudate is thought to result from the rupturing, which can spread throughout the brain. This exudate is a thick, gelatinous substance that has a high density. The exudate is thought to be the cause of most of the complications associated with TBM (Andronikou *et al,* 2004).

At present TBM is very difficult to diagnose when a patient first presents with symptoms. As mentioned above, there are a wide variety of tests available to the clinician. The disadvantage of these tests, are the need for invasive procedures, the time taken to obtain cultures and the fact that many prove inconclusive. Imaging technologies such as cranial computed tomography (CT) of the brain and magnetic resonance imaging (MRI) are having more widespread use in the diagnosis of TBM.

2.2 Computed Tomography

CT involves the use of a collimated x-ray beam and a detector system to measure x-ray attenuation (absorption and scattering) for a series of projections of the beam through the patient (Stimac *et al*, 1992). This principle of CT is what enables us to use the technology to measure density of different tissues in the body. The tissues in the body absorb different amounts of radiation, the amount of radiation absorbed gives an attenuation reading and this is scaled to different grey values and displayed on the screen of the CT machine. Dense tissue such as brain matter absorbs more x-rays, has a high attenuation and is displayed as white on the computer screen. As the tissue becomes less dense or absorbs less x-rays it is displayed as a grey value and eventually in the case of air, it is displayed as black.

The CT x-ray tube differs from a conventional tube in that it rotates around the patient. The beam used is a thin fan shaped beam that irradiates a thin slice. Multiple detectors around the patient measure the attenuated x-rays and are reconstructed, giving a complete slice through the patient. The intensity of x-rays received by the detector is equal to the initial intensity (I_0) reduced by the amount absorbed by the patient according to the law of x-ray attenuation:

$$I = I_0 \exp[-\mu L]$$

Where μ is the linear attenuation coefficient (dependent on the type of tissue and the energy of the x-rays) and L is the x-ray path length.

For computed tomography, where the image has a depth dimension this equation is modified for use with a voxel (a box with a side of 1mm and thickness determined by the beam collimation). The modified equation gives the received intensity (I) at the detector which is the initial intensity reduced by the attenuation that occurs in each voxel:

$$I = I_0 \exp[-(\mu_1 + \mu_2 + \mu_3 ... + \mu_n)dL]$$

where *dL* is the length and width of each voxel and the μ values are those of each voxel along the path (Stimac, 1992). By adding up the attenuation coefficients in the exponent, the tissue density for each voxel can be determined. Reconstruction of μ is made on a rectangular array when creating an image, with each pixel having a different value of linear attenuation. Before displaying these, the values are usually scaled or normalized.

This gives what is commonly known as the CT number of Hounsfield units and is defined by:

$$\text{CT number} = \frac{\mu_{\text{tissue}} - \mu_{\text{water}}}{\mu_{\text{water}}} \times 1000$$

From the above equation the CT number is the fractional difference of its linear attenuation coefficient relative to water, measured in units of 0.001 (Webb, 1992). The CT numbers of soft tissue are relatively close together, but the user can choose to display the CT numbers in any way. The average screen can only display 256 colours of grey; therefore the radiologist can choose a window level specific for the tissue he/she is interested in. For soft tissue, most of the CT numbers are close to zero so a narrow window level is chosen in order to amplify the contrast of the display. In other words the output brightness on the screen is related to the CT number by means of a level and a width control.

2.3 The role of CT in diagnosis of TBM

To understand how CT aids in the diagnosis of TBM it is important to have a basic knowledge of the brain Anatomy. Below in Figure 2.1, the CT image shows some of the basic anatomy relevant to TBM. The basal cisterns are closed spaces in the brain that serve as reservoirs for Cerebro-spinal fluid, they are named for their location in brain. A few of the basal cisterns are highlighted, but it is impossible to show all of them since they appear at different depths in the brain and multiple CT slices would be necessary to show them all.

2.3.1 Brain anatomy

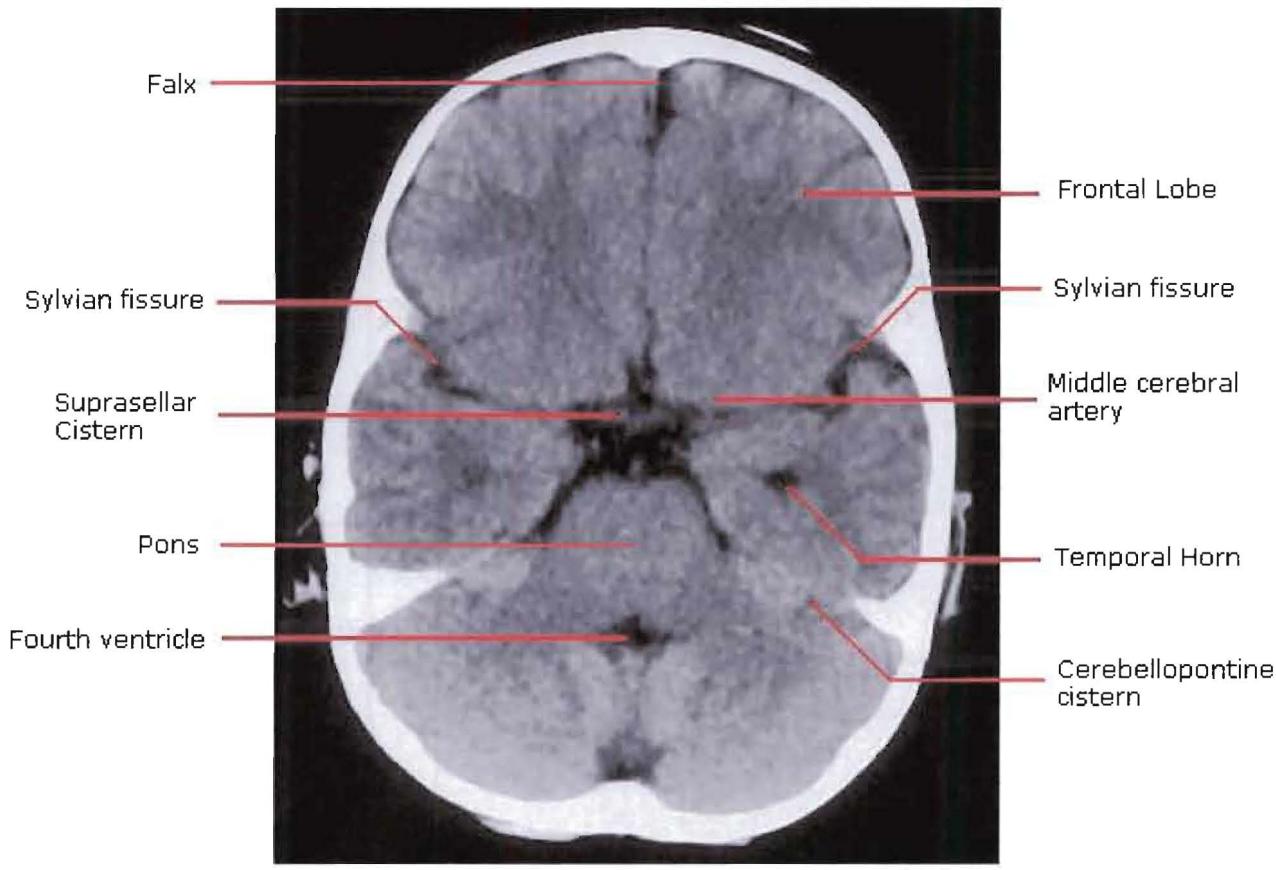

Figure 2.1 A CT image taken at the level of the fourth ventricle, highlighting certain anatomy of the brain relevant to TBM

CT has been shown to be one of the most important diagnostic methods in the assessment of TBM and its complications (Ozates *et al*, 2000). Although many studies have been done, the literature remains contradictory on certain points, but there are a number of signs that are looked for when patients present with possible TBM. Some of the more important signs are mentioned below, with findings from different papers being presented for comparison.

2.3.2 Hydrocephalus

The first sign we discuss, is the one for which there is most agreement. Hydrocephalus is the swelling of the brain ventricles which contain CSF. Many reasons for this have been submitted, but the most likely is that the TBM exudate forms adhesions of the basal subarachnoid space. This blockage in the cisterns prevents the CSF from flowing from one ventricle to the next, and so the ventricle that is blocked starts to swell with CSF and is therefore classified as hydrocephalic (Thwaites *et al,* 2000). Figure 2.2 compares the normal ventricles size to a ventricle that has been enlarged due to hydrocephalus.

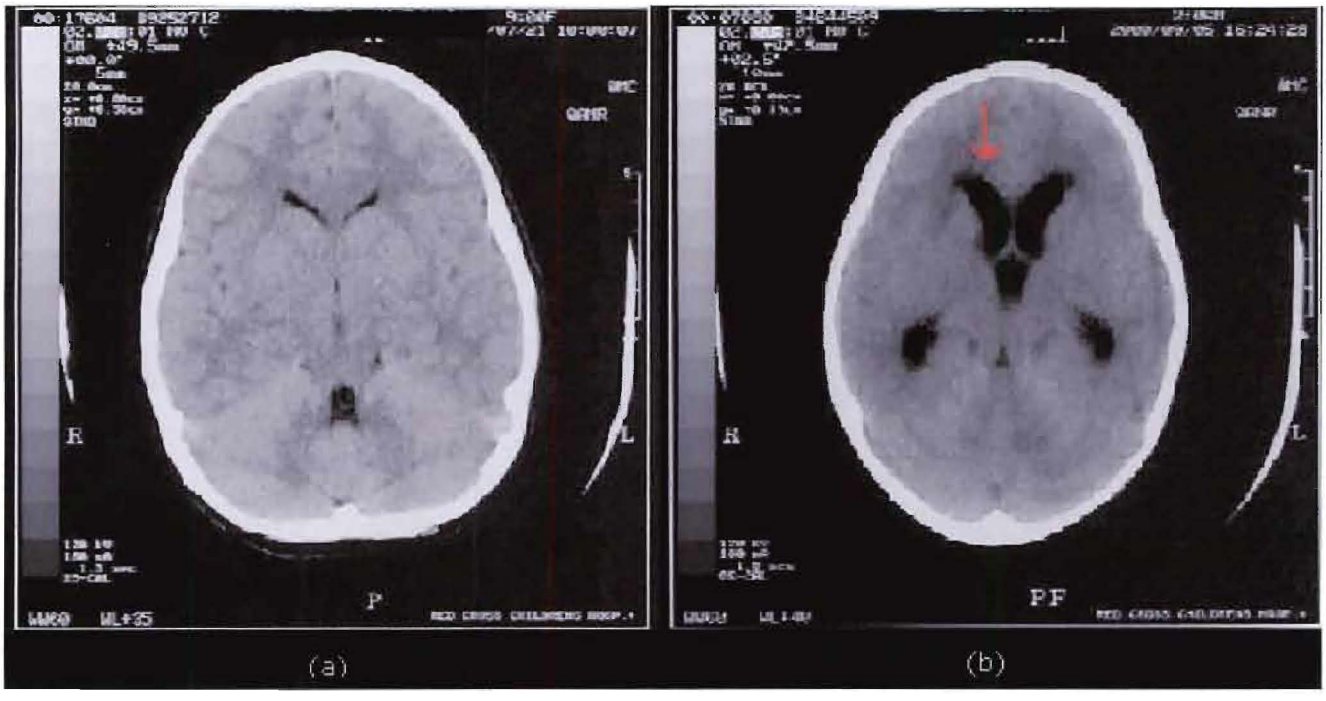

Figure 2.2 : Showing the difference between the ventricle sizes in (a) a normal patient and (b) one with hydrocephalus

Image (a) in Figure 2.2 shows the normal size of the ventricles. Image (b) shows the presentation of hydrocephalus when imaged using CT. The red arrow indicates the abnormally swollen ventricles that are pushing on the surrounding brain tissue, which may cause irreversible damage. 80% of the children in one study showed the presence of hydrocephalus and this may have been caused by an obstruction at the level of the basal cisterns, (Kingsley *et al*, 1987).

Hydrocephalus was found in a similar 80% of 214 patients in a later study (Ozates *et al*, 2000). It is also clear that hydrocephalus can vary according to the stage of the disease and is most likely to present with other signs. Hydrocephalus alone is not exclusive to TBM and therefore cannot be used in order to diagnose TBM.

A recent study by Anronikou *et al* (2004) found hydrocephalus associated with TBM less frequently than the other studies, with only 67.6% of the patients showing signs of hydrocephalus.

2.3.3 Basal Enhancement

Basal enhancement is important to our study as it is similar to the sign we are trying to detect. The use of contrast enhancement is the only method at present of viewing basal enhancement. Once the contrast dye has been injected, the blood vessels and hyperdense tissue in the brain show up as whiter in colour when seen on a CT image. Most children that are sent for CT scans because TBM is suspected, are under 3 years of age and therefore any invasive procedure should be avoided due to patient safety concerns. Contrast enhancement also adds to the cost of scanning, and this, in addition to the risks associated with the invasive nature of contrast injection, motivate the search for other signs of TBM.

Figure 2.3 below shows the enhancement of the blood vessels and certain regions of the brain.

Figure 2.3 : Image showing example of basal enhancement in the post-contrast scan of a patient with TBM – the red arrows indicate enhanced areas.

The presence of basal enhancement is debated in many of the previous studies. In one of first TBM studies (Kinsgley *et al,* 1987) the presence of basal enhancement was found in 75% of children that were admitted with TBM.

One of the largest studies of 214 children with TBM showed basal enhancement to be as low as 42% (Ozates *et al*, 2000).

In a more recent study by Kumar *et al* (1999) it was shown that basal enhancement with or without tuberculoma was present in 90% of children with TBM.

The study by Andronikou *et al* (2004) revealed basal enhancement as the most common sign associated with TBM with 89% of the patients showing signs of enhancement.

Although the high prevelance of basal enhancement is disputed, it has shown itself as a sign that is well linked to TBM and is definitely helpful in diagnosis, with all studies associating the presence of basal enhancement with TBM.

There are many reasons for the differing results in the studies, the most obvious being that CT scans for different patients were read when the disease was at different stages of progression. Radiologists are trained to see the enhancement of various tissues and rate it as to its severity or whether it is pathological. Detection of mild enhancement is thus dependent on the radiologist examining the images, and experience plays a major part in diagnosis.

Once important conclusion from all the studies is that basal enhancement with ventricular enlargement (hydrocephalus) was a feature of advanced TBM with a poor prognosis (Ozates *et al,* 2000).

2.3.4 Cerebral Infarcts

Cerebral Infarction is the death of the cells in the brain, and is thought to result from the occlusion of blood vessels that feed the brain tissue. The combination of the exudate from the TB and swelling of the brain meninges is thought to compress the vessels and prevent the flow of blood to the cells, therefore causing their death.

Infarcts present as dark patches in otherwise normal brain tissue, and may be difficult to detect when in close approximation to the ventricles. Figure 2.4 below shows the common pattern of infarction associated with TBM. The arrow shows the dark area below the lateral ventricle indicating an infarct.

Figure 2.4: Image showing the presence of an infarct in a patient with TBM – indicated by the arrow

The literature reveals a large range in the incidence of infarcts, and associates them with late stage of the disease. Kinglsey *et al* (1987) found that 67% of patients had infarcts, but the later study by Ozates *et al* (2000) found that only 13% of the children with TBM had signs of infarct.

The latest study by Andronikou *et al* (2004) found similar results to Kingsley *et al* (1987) with 62% having infarcts. Nearly all TBM patients with basal enhancement have been found to have associated infarcts (Andronikou *et al,* 2004; Kinglsey *et al,* 1987; Ozates *et al,* 2000).

2.3.5 Granulomas or Tuberculomas

The last of the well documented CT signs of TBM is the presence of a Tuberculoma. Tuberculoma are not seen as frequently as the other CT features of TBM and are only helpful in supporting the diagnosis. Granulomas are the result of the TBM infection becoming ulcerated. It forms an inflamed mass of granulated tissue that has a high density. Tuberculoma is the name given to a granuloma caused by the TBM infection.

The Tuberculoma shows up on a CT scan as a white circle, due to its hyperdensity and can often have an outer ring-like layer. Figure 2.5 below gives an example of what a Tuberculoma may appear like on a brain CT. Their presence can be found throughout the brain, but is most common closer to the meninges covering the brain.

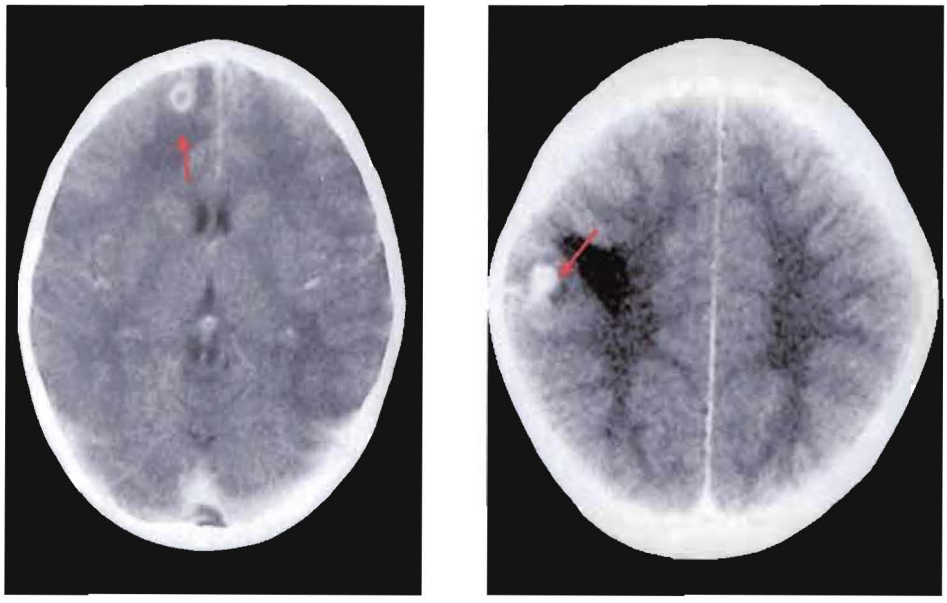

Figure 2.5: Showing 2 examples of Tuberculoma presentation for patients with TBM. The arrows point to the location of the Tuberculoma.

Tuberculoma are the least common sign associated with TBM. Their presence ranges from 5% to 16% and they are therefore absent in most cases (Ozates *et al,* 2000; Andronikou *et al,* 2004).

Nearly all the signs mentioned above that are used in diagnosing TBM are subjective.

What is needed is a quantitative measure that could be applied to the images to help flag possible abnormalities in the brain, therefore leading to earlier treatment. In order to do quantitative work a measure of density of the tissues will be necessary, and so we proceed with a review of the literature on soft tissue densitometry. Figure 2.6 below shows the typical signs associated with TBM.

Figure 2.6: Showing CT scans from 2 different patients, (a) shows a normal brain scan. (b) shows clear signs of TBM. Note the large ventricle size and enhanced tissue in the oval area. Both images are taken from patients presenting at Red Cross Children's Hospital

Figure 2.6, (b) shows an example of a TBM patient showing multiple signs associated with the disease. The higher the number of signs in the image, the stronger the case for TBM.

2.4 Soft Tissue Densitometry

The use of CT in soft tissue densitometry has not been well researched. Few papers have been published as it is widely believed that CT cannot be used to indicate an absolute density, due to the fact that the CT numbers vary significantly from one scanner to the next when differing settings are used. Also the CT numbers of certain substances such as fluids, blood, abscess and tumour overlap and therefore should not be used as absolute values (Stimac *et al*, 1992).

The sources that cause the CT numbers to differ from patient to patient and one scanner to another are many in number. Some of the factors are the actual components of the scanner, and others result from differing tissue makeup in separate individuals. Other sources include age, which has a non-constant effect on tissue density and varies from person to person, and is therefore difficult to take into account. The amount of blood flow in a tissue at any one time also changes the density value of that tissue. The volume of fluid in a cavity is also seen to influence the CT numbers of the region of interest (Laurence *et al*, 1983).

The literature does state that a comparison of CT numbers in different structures in the same patient is reliable and reproducible, and this is a possibility that can be exploited when estimating density of tissues (Phelps *et al,* 1975).

2.5 Factors influencing quantitative use of CT numbers

CT numbers as absolutes are hardly ever used today. A range of CT numbers is what most radiologists usually assess. There are a number of reasons why an absolute CT number cannot be used, and some have been discussed already.

To understand fully why these numbers can't be used as absolutes, an examination of early CT work is needed. Researches initially believed that they would be able to classify a disease or

tumour by its characteristic CT number. However this idea was laid to rest when researches discovered that even healthy tissue had a large variation in CT number. Phelps *et al* (1975) found a promising correlation between attenuation co-efficients of various tissues and CT numbers. Several studies suggested that quantitative measures are not accurate enough *in vivo* as the differences in attenuation co-efficient of certain diseases were small and overlapping (Zerhouni *et al*, 1982).

Work by Zerhouni *et al* (1982) discussed the use of absolute CT values in evaluating solitary pulmonary nodules (SPN), and concluded that multiple parameters can change the CT value. He then set about trying to establish what those parameters were. What he discovered can be applied universally to other objects in the body and the main parameters are discussed below.

The use of different reconstruction algorithms has a large effect on the CT number. When the Zerhouni study was done, the main method of image reconstruction was filtered backprojection, where each image was first subjected to spatial frequency filtration and then projected back into the time domain onto an image plane. The use of backprojection speeds up the process of image reconstruction as the signal in the frequency domain is decomposed into its original sine and cosine functions, on which arithmetic operations are easily performed.

Due to the mathematical transformation used, when sudden changes in the density of material are encountered, 'overshoot' or 'undershoot' artifacts may be generated. These errors are an intrinsic feature of the mathematical transformation used in CT algorithms. For example when going from an area of high density such as bone to a possible infarct, the large variation in density can cause an error at a point by up to 9% of the difference in density values between the edges of two differing density points (Zerhouni *et al*, 1982). This would mean that the edges between the bone and infarct could be sharper than normal due to the overshoot error.

Especially in more modern scanners, different manufacturers use different algorithms for reconstructing the CT image. This leads to a variation in 'overshoot' or 'undershoot' error from one scanner to the next.

As the x-ray beam passes through the body, the lower order x-rays are attenuated, causing the mean energy of the beam to increase. This phenomenon is called beam hardening (Rao *et al*, 1981). Therefore the same tissue may attenuate less of the x-rays near the centre of the body as the energy of those x-rays are higher, resulting in lower CT numbers towards the centre of the body.

Current CT scanners have built in beam hardening correction for head CT which will reduce this artifact for our purposes. The tissue most affected by beam hardening is skull due to its high density. Although the correction used by most CT scanners to overcome beam hardening is effective, not all artifacts can be corrected exactly.

Factors such as milliamperage, and time that the x-ray beam remains on for can affect the CT numbers, but are thought not to be significant. On the other hand variations in kilovolt potential of the beam has large effects on the CT numbers. This variation is due to the fact that different beam energies alter the attenuation because of the changes in the importance of photoelectric and Compton effects (Zatz *et al*, 1977).

An important technique when examining this change in attenuation corresponding to different beam energies is the use of the dual kVp technique. This technique involves imaging the same area twice with different voltage potentials for each image. This technique has been demonstrated to be successful when applied to the brain to differentiate blood clots from contrast enhancement (Marshall *et al*, 1977).

Phelps *et al* (1975) investigated the attenuation coefficients of various substances at differing beam potentials. Potentials from 18 to 136keV were used and the attenuation coefficients derived by using the formula below.

$$I = I_0 \exp[-\mu L]$$

This study is relevant to our work as the attenuation coefficients of CSF and other brain tissues are well documented by Phelps for differing potentials, and may be useful in calculating the density of the tissues or the CSF.

The final result of the study by Zerhouni *et al* (1982) indicated that a threshold value could be used, to classify whether a solitary pulmonary nodule was benign or not. They determined that any nodule having a CT value higher than 164 HU was considered benign. This result is very important as it proves that CT of soft tissue can be used to classify a disease or a tumour, by looking at a range of CT values, and after having taken certain artifacts into consideration.

2.6 Quantitative CT values from brain tissue

Very few papers have been published dealing with quantitative brain CT values. A paper by Fike *et al* (1982) attempted to segment areas of the canine brain using CT numbers. Of the five anatomic regions selected for measurement, the most relevant for our work is that of the midbrain. Both pre- and post contrast scans were used, and the area of interest was delineated using the region of interest (ROI) control on the CT scanner. From the regions of interest, the CT numbers were measured and compared. They found that for smaller ROI the CT values were more variable and less reproducible, with differences ranging from less than 1 to slightly greater than 4 HU. This was due to the fact that noise in the image exists as speckle. When a larger number of pixels are examined, the noise is averaged out. For small regions of interest eg: 2 pixels, if one is a noise pixel, the combined CT value of the two pixels will be inaccurate.

The study found that the excellent spatial and contrast resolutions inherent in CT systems facilitate a quantitative as well as qualitative appraisal of canine brain morphology. Also of importance is that although the CT values of various regions in the brain were similar, the densitometry measurements from the pre-contrast scans were able to differentiate the various tissues. The variability when using a smaller ROI means that a larger range of values would be needed to classify a tissue as normal or abnormal.

These normal values could be used to diagnose pathologies which affect the density of the brain tissue. This result leads us to believe that the method could be applied to the human brain in detection of TBM since TBM does have an effect on the normal tissue density.

2.7 Tissue Segmentation in Medical Images

Being able to differentiate different tissue types in medical images is important in diagnosis. In the past most tissue segmentation was done by the radiologist simply using his/her eye to differentiate between the different tissues in an image. Computer aided segmentation will greatly assist radiologists in their diagnosis when distinctions between tissue types are not easily observed by the human eye.

Grey tone images contain uncertainty due to each pixel having possible multivalued levels of brightness (Bezdek *et al,* 1992). This is due to inherent vagueness in the images and is made up of the uncertainty associated with the greyness and also uncertainty of the spatial qualities. The uncertainty results from the process of digitising an image and that when digitised the image intensities must be represented by integers. The spatial ambiguity refers to the uncertainty in the shape and geometry of a region in an image. Medical images are good examples of images containing uncertainty due to variations in anatomy between patients, variations in scanning parameters, and in some cases unclear boundaries between different types of soft tissue. In conventional clustering, allocations are based on 'crisp' decisions (i.e yes or no). This means that conventional clustering is not well suited to medical images that contain uncertainty and should be modelled in a different way.

Clustering is a useful method of image segmentation. Many different types of clustering have been performed, from thresholding to k-means clustering and fuzzy clustering. Clustering essentially seeks to segment the pixel brightness or density into clusters of similar density. Rajapakse *et al* (1997) classified the different methods of clustering into four subgroups.

1. The classical methods
2. The statistical methods
3. The neural network methods
4. The fuzzy clustering methods

In a study by Nevin *et al* (1999), comparisons were made of the different methods, by quoting results from various papers. The classical methods, such as thresholding and edge based techniques were the least successful methods of segmenting medical images.

The statistical methods, such as the maximum-likelihood-classifier (MLC) gave satisfactory results but were reliant on prior knowledge and subject to error if the initial clusters weren't well positioned.

The neural network methods proved to be more successful than the statistical and classical methods, but still had difficulty with the uncertainty which is inherent in medical images.

The final type of method reviewed was fuzzy clustering. The results compared well with those of neural networks, although certain algorithms took longer to segment the image than neural networks and were sensitive to noise.

2.8 K-Means Clustering

The most simple and quickest type of segmentation to implement is classical segmentation, where k-means clustering is a good example. The process involves segmenting an image into a given number of clusters, therefore making it a supervised algorithm. Supervised algorithms rely on prior knowledge of the image densities, as the number of clusters must be chosen before the image is segmented. The algorithm picks initial density values for each cluster that the image is to be divided into. It then computes a simple Euclidean distance between each pixel in the image and each cluster centre.

Each pixel is then assigned to the cluster of which the centre is closest to it. Once this is complete the average density for each cluster is computed and this becomes the new cluster centre. The process is repeated and keeps repeating until the cluster centres do not change. After the process is complete, the image will be divided into a number of clusters of equal densities and therefore segmented (Coleman *et al*, 1979). Although k-means is an effective clustering technique, it has limited applications to segmenting medical images. The uncertainty in the images makes such hard clustering an inaccurate method of segmenting medical images.

2.9 Fuzzy Logic

Fuzzy sets were first introduced by Zadeh (1965) as a way of representing uncertainty or vagueness in real world problems. Fuzzy models essentially attempt to capture and quantify non-random imprecision (Bezdek *et al,* 1992).

With conventional set theory, each object or number in a set satisfies an exact property to have membership to that set. For example, the conventional set of numbers between 5 and 10 is a crisp or conventional set. The membership function for the set can be written:

$$M_H(t) = \begin{cases} 1; & 5 \leq t \leq 10 \\ 0; & \text{otherwise} \end{cases}$$

From the equation above, it is evident that every object in this set either has the value 1 or 0, therefore making it a crisp set.

Fuzzy sets have a way of representing imprecise data by mapping each number in the set into the interval [0:1]. For an example relevant to this project we look at the case of a CT image. The image is made up of a number of pixels having different grey values. The image can be regarded as a fuzzy set, and each pixel can be regarded as having a value that represents its fuzzy membership to the set.

The borders of the set are 0 which represents the colour white, and 1 which represents black. Therefore a pixel having grey value 0.8 has a high fuzzy membership to the colour black.

From this example we can see that fuzzy sets are ideal for working with medical images, where uncertainties are present and boundary conditions are difficult to detect using conventional 'crisp' sets. By using fuzzy logic, the vagueness can be represented and therefore a more accurate representation of the problem can be generated using fuzzy logic.

2.10 Fuzzy C-Means Algorithm

Cluster analysis is based on partitioning data into a number of subgroups or clusters. The objects located within each cluster must show a degree of similarity. In hard clustering such a k-means, each point in the data is assigned to only one cluster. With the use of fuzzy clustering, each pixel has some degree of membership to each cluster. The degree of membership is an indication of how similar or close a pixel is to some criterion (Gath and Geva, 1989).

Bezdek (1973) developed a clustering algorithm based on fuzzy extension of the least-square criterion and proved the convergence of the algorithm to a local minimum. This algorithm stands as the basis for all fuzzy clustering and little has changed from the original. The fuzzy c-means algorithm can be regarded as a pixel classification scheme. Each pixel is classified and segmented according to its grey value in the image.

The advantage of the fuzzy c-means method over other methods of segmentation such as classical and statistical, is that the algorithm does not require any prior knowledge of the data and it is fairly robust to noisy data.

The fuzzy c-means algorithm by Bezdek *et al* (1973) is based on minimization of the following objective function, with respect to U, a fuzzy c-partition of the data set X, and to V, a set of cluster prototypes.

$$J_q(U, V) = \sum_{j=1}^{N} \sum_{i=1}^{K} (u_{ij})^2 d^2(X_j, V_i); \quad K \leq N \qquad (1)$$

In equation (1), J is the objective function to be minimised. U is a fuzzy c-partition of the data set. The value q is any real number greater than 1 and is a weighting exponent on each fuzzy membership. The weighting exponent q allows us to alter the 'fuzziness' of the equation. The higher the value of q, the 'fuzzyier' the equation becomes. If the value of q is 1 the equation simply becomes the k-means clustering algorithm. X_j is the jth m-dimensional feature vector or data point in this case, V_i is the centroid of the ith cluster. u_{ij} is the degree of membership of the data point X_j in the ith cluster, $d^2(X_j, V_i)$ is any distance measure between the cluster centre V_i and the data point X_j, N is the number of data points , and finally K is the number of clusters.

To create a fuzzy partition of the data, iterative optimization of equation 1 needs to be carried out.

This is done by the following steps:

1. Choose primary cluster centres V_i - This can be done randomly, or initial estimates might be chosen by examining the histogram of the image.
2. Compute the degree of membership of each data point to all the clusters

Membership is calculated from equation 2 below:

$$u_{ij} = \frac{\left[\frac{1}{d^2(X_j, V_i)}\right]^{\frac{1}{(q-1)}}}{\sum_{k=1}^{K}\left[\frac{1}{d^2(X_j, V_k)}\right]^{\frac{1}{(q-1)}}} \qquad (2)$$

3. Compute new cluster centres $\hat{V}_i$ according to equation 3 below:

$$\hat{V}_i = \frac{\sum_{j=1}^{N} (u_{ij})^q X_j}{\sum_{j=1}^{N} (u_{ij})^q} \qquad (3)$$

Once the new clusters have been calculated, the degree of fuzzy membership must be updated from u_{ij} to $\hat{u}_{ij}$

4. Check the termination criterion to determine whether another iteration is required. The criterion is given by equation 4:

   If max $\left\| u_{ij} - \hat{u}_{uj} \right\| < \epsilon$, where ϵ is a termination criterion between 0 and 1 (4)

Once the error criterion is reached, the iterative process is complete and the data is separated in a fuzzy partition. From equation 2 when calculating the degree of fuzzy membership, the distance measure $d^2(X_j, V_i)$ is used. When the distance measure represents the Euclidean distance, the fuzzy c-means algorithm is the result. There are many algorithms that make use of different distance measures and all have their own unique name according to the distance measure.

There are a number of definitions for data to be part of a fuzzy subset. According to Banerjee *et al* (1999) a fuzzy c-partition is defined as a V × N matrix U, where V and N represent the same as in equation (1) such that:

- Each row U_i is the ith fuzzy subset of X
- Each column U_j exhibits the membership grades of datum j in every fuzzy subset
- The sum of membership grades of each datum in all of the fuzzy subsets, is unity
- There is no empty fuzzy subset
- No fuzzy subset is all of X

The final result is an image partitioned into the number of clusters, the number of clusters was chosen by the user before running the algorithm. Each pixel in a cluster has a degree of membership associated with it. This degree of membership is an indication of how closely that pixel is associated with its cluster and is a number between [0,1]. When the number is high, eg 0.98 that pixel is strongly associated with that particular cluster, but still leaves a degree of uncertainty. To separate the image into partitions, the algorithm looks at the degree of fuzzy membership to each cluster, and assigns the pixel to the cluster that has the highest degree of membership.

3 QUANTITATIVE EVALUATION OF HYPERDENSITY

It had been hypothesized that patients with TBM have hyperdense CT values in certain areas of their brain scans. In order to verify this hypothesis, we proceeded to reconstruct these CT values in order to prove the presence of hyperdensity.

3.1 Data Format

The patient base was children presenting at the Red Cross Children's Hospital in Cape Town with signs of TBM. All the patients had full laboratory work-ups and both pre and post contrast CT brain scans. The patients were separated into 3 categories: The 'definite' category consisted of 37 children with an average age of 24 months. All these children had confirmed TBM from culturing of a CSF sample. The 'negative' group of patients had 32 children who had subsequently been diagnosed with something other than TBM. Finally the 'probable' group contained 93 children with most of the clinical features of TBM but the laboratory had failed to isolate TBM from the CSF. This did not exclude the patients from having TBM.

All the CT scans that were used in the study were captured on a General Electric Prospeed Fast S scanner (Yokohama Medical Systems, Japan). The technique used to scan the patients was a standardized procedure for brain scanning which included 5mm slice thickness of the posterior fossa and 10mm slices above that. The window settings were also standard and the level was set to 35 and the window width to 60.

Once the images were created by the CT machine, they were printed onto film to be stored as hardcopy images and were only stored in their original softcopy format for 1 month due to the high volume of patients seen in the CT unit and the expense to keep them in this format. In order to further reduce the costs when printing the films, all images in the sequence for each patient were reduced in size and printed on 1 film, which resulted in approximately 16 images per film.

3.2 The Hypothesis

Hyperdense exudates in the basal cisterns were found by 3 expert radiologists in 17 of the 37 cases in the "definite TBM" category of the scans used in the project (Andronikou *et al,* 2004). These findings were subjective as the radiologists were not able to verify quantitatively what they assessed as hyperdense areas of the brain scans.

The exudate that is expelled into the cisterns of the brain when TBM is present, is a thick grey, high density substance. Because of its high density, it shows up as brighter than normal brain tissue when seen on a CT image. Depending on the amount exuded, the higher density may be obscured by the surrounding tissue and difficult to differentiate as whiter than the surrounding medium on a CT image.

When CT images in digital format are displayed on the viewing screen of the scanner, what is shown is a scaled attenuation co-efficient, or a measure of density for each pixel displayed as a grey scale image. Therefore when the image is in digital format, doctors are able to select any image pixel and the corresponding CT number or density for that pixel can be displayed. With digital images it is simple to obtain a quantitative value that can verify whether a pixel is hyperdense or not. Unfortunately this density information is lost when the images are printed as was done for the patients in this study.

Hardcopy films needed to be converted back into digital images that could be measured. A technique was therefore needed to obtain CT numbers from these scans in order to validate the hypothesis that patients with TBM have areas of hyperdensity in their brain CT scans.

3.3 Reconstruction of the CT numbers

CT images generally contain 4000 CT numbers, but the average computer monitor is only able to display a limited percentage of these, and the human eye can only distinguish approximately 16 different grey values. Due to this limitation, images need to be scaled in order to show the best contrast for the observer. This is accomplished through setting window levels and width, and is crucial in reconstructing the CT numbers from the hardcopy films.

3.3.1 Windowing

When the computer is required to display a CT image, the digital CT values are read from their stored location and on older equipment without digital displays, converted to analogue signals for display purposes. To alter the way the image is displayed, a look-up table (LUT) is used that converts the CT values to a range of 256 shades of grey that are displayed as the image (Bushberg *et al*, 1994).

For most CT scanners the LUT is represented by a simple ramp function that scales the CT values. The width of the ramp function is the window width and the midpoint value of the ramp function is the window level setting. The slope of the ramp represents the contrast in the image, therefore increasing the slope by decreasing the window width increases the contrast of the image being displayed. The window width represents the number of CT numbers that can be displayed. The left edge of the ramp function starts at (Window level – Window width/2) and similarly the right edge of the ramp ends at (Window level + Window width/2). This means that any CT number lower than the value on the left edge of the ramp, will be displayed as black or 0 and any CT value higher than the right edge will be displayed as white or 1.

By changing the window width and level it is possible to get maximum contrast for the desired tissue. On most modern scanners the desired tissues have standard window levels and width for optimum display. For example most brain tissue has a low density and so the window width is set at 60 CT values and centred around the window level 35. Shown below in Figure 3.1 are the window level and width for the brain.

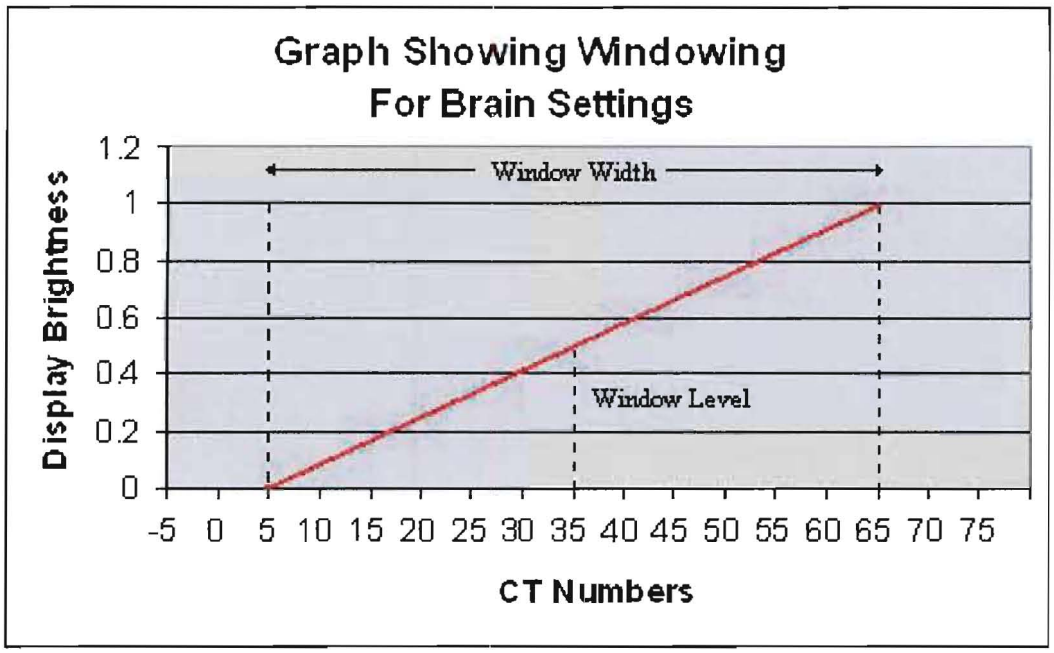

Figure 3.1: Graph illustrating the window settings for brain tissue

3.3.2 Hardcopy to Softcopy Procedure

In order to apply an algorithm to the data, the hard images were converted to digital images by high grade medical scanning.

All of the hardcopy images were scanned using a Cobra CX 612T scanner at the Kuilsrivier hospital. The scanner provides high definition scanning and image formats that were suitable for use in this project.

The images were scanned and saved as jpeg files in order to reduce the size of the files. The films were scanned at 300dpi resolution to provide optimal quality, using the 12-bit greyscale scanning mode. The average size of the image was 4200 pixels wide and 5093 pixels long. This image size was clearly too large for our applications as the file size was approximately 40 to 60 megabytes and each CT slice was larger than the viewing monitor. They were resized to a more

manageable size of approximately half the original i.e: 2065 pixels wide by 2510 long. Each image contained approximately 12 to 16 separate brain images at different depths in the brain.

In order to reduce the large number of images produced for each patient, CT images which were not of relevance to the study were discarded. Since some areas of the brain do not show signs of the disease, they are not of value and would waste large amounts of computational time. With expert consultation some of these were excluded from the project.

The area of the CT scan outside of the brain is of no use as it provides no relevant information and in order to further reduce computational time for the algorithm the images were cropped.

3.3.3 Algorithm Implementation

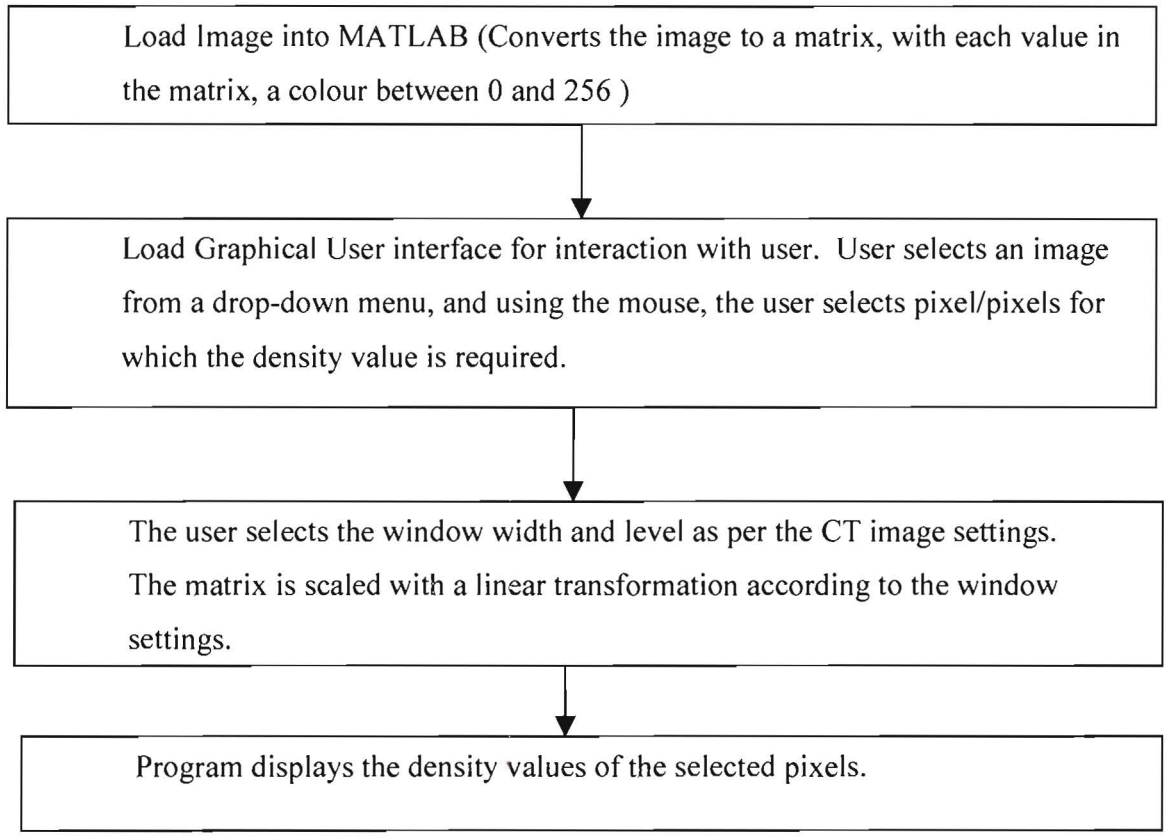

3.3.4 Graphical User Interface

The need for the graphical user interface arises from the fact that physicians require minimal interactions with the workings of the program. The interface was designed to compliment the users' previous knowledge of working in Windows.

Most radiologists are familiar with working in Windows-based programs, thus it would be intuitive for them to have a system that utilizes similar pull-down menus and selection using a mouse.

On loading the program, the user is presented with a number of choices. Figure 3.2 below shows the menu the user is presented with when loading the program. Firstly the user selects the desired CT image from a drop-down menu. The image is loaded and appears on the screen. The user must then select the appropriate window level and width by entering them into the provided boxes. Using the mouse, the user selects "Get density values".

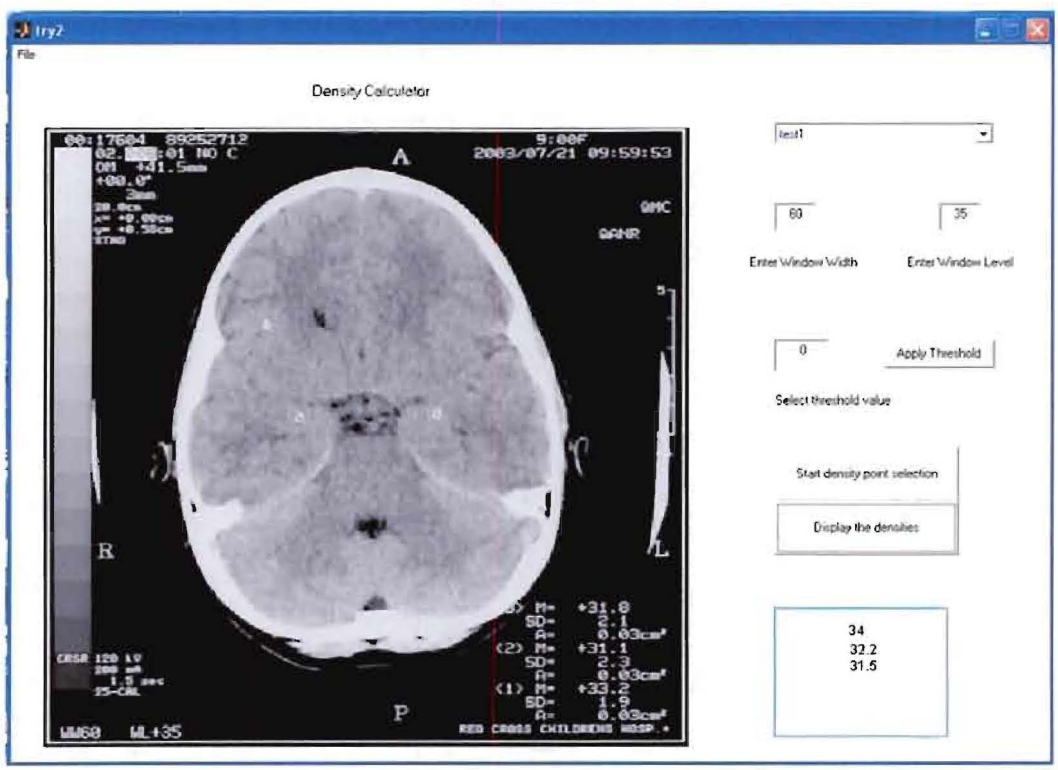

Figure 3.2: Showing the user interface screen

Figure 3.2: Showing the user interface screen

The user then positions the cursor over the desired area in the image and presses "Enter". The algorithm then computes the linear scaling and outputs the density value to the screen for the selected pixel, which can then be compared to normal brain CT numbers to determine if it is hyperdense.

Another button 'Apply threshold' and a box for choosing the threshold value are included in the program. This enables the user to select a value that he/she believes to be the upper limit of normal tissue. By clicking on 'Apply Threshold' all values lower than the selected threshold value are set to black, and therefore only the tissues that are hyperdense remain.

3.3.5 Linear Mapping

Once the CT images have been scanned into the computer, they are saved as jpeg format images, which reduces their size without diminishing the quality of the images noticeably. When the images are imported into Matlab and converted to greyscale images, they are converted into 256 colour format.

The window width displays the number of grey values that were originally displayed in the image when it was created. The window level indicates the density value around which the window level was centred. As mentioned in section 3.3.1 the window level used in most of the images in the project was 35 and the window width was 60. From these we can deduce that any density value less than 5 in the original image was displayed as black and any density value higher than 65 was displayed as white.

From this it simply follows that the pixels in the scanned images consisting of 256 colours must be scaled to the density values 5 - 65, therefore providing a density value for each pixel in the new image.

The equation implemented in the algorithm is as follows:

$$\text{CTnumber} = \left(\text{WindowLevel} - \frac{\text{WindowWidth}}{2} \right) + \text{pixelColour} \times \frac{\text{WindowWidth}}{256}$$

3.3.6 Limitations of Reconstruction

The nature of the hardcopy film ensures that certain data in the original digital images is unrecoverable. Any pixels in the original image that fell outside the window range could not be reconstructed to any accuracy as the data was lost when the image was printed. The algorithm is therefore only accurate for tissues with densities that fall within the window limits. All tissues having either higher or lower density values will be displayed as the maximum or minimum window setting. These limitations did not impact on this project as the required density values consisted of brain matter which fell in the window settings that had been chosen.

Although not exact duplicates, the error between the reconstructed and original densities has been proven to be statistically insignificant, by a correlation test. Therefore they may be used in order to prove the results. Details of the correlation test is found in section 3.4.2

3.3.7 Errors Introduced to the Images

Different factors contribute to the overall accuracy of the reconstructed densities at different stages of the reconstruction chain, and need to be addressed separately in order for their overall effect on the density to be understood.

The first and most obvious factor that introduces error into the chain is the fact that the images are in hardcopy. When the images are converted from the digital versions on the CT scanner to the films used by the radiologist for viewing some information is lost.

When the images are printed to film, they are immediately exposed to outside agents such as dust, heat and sunlight that can affect the film itself and lead to error being introduced. The films are sealed as they emerge from the printer, but over a number of years the film starts to decay and so accuracy and subtle grey value differences may be affected. Fortunately most films used in this project were less than 4 years old and had been stored correctly so that these factors should have had very little impact.

The scanning of the films to convert them back to digital format is the part of the process that introduces the most error. Even though a medical grade scanner was used with high resolution scanning, it is not possible to recreate the original digital image exactly, or the appearance of the hardcopy.

To totally eliminate error, the light source in the scanner needs to be completely uniform which is impossible to achieve, and no extraneous light must be allowed into the scanner while scanning, which again is impossible to achieve. Although the noise introduced to the images at this stage may be more significant than at any other stage, it is mostly uniform noise and applies to all images that are scanned. As we are comparing images that were all acquired using the same technique it is possible to disregard the noise as it affects all the images in the same way. Comparison to images acquired from a different CT scanner, different film and another type of scanner would be unreliable as the noise introduced would also differ.

For non-uniform noise, there is little that can be done to correct the image. Certain algorithms may be applied to fix contrast inhomogenities, but they may change correct areas as well, which is undesirable.

3.4 Validation of the algorithm

Validation of the algorithm used to reconstruct the CT numbers was based on comparison of reconstructed values with known CT numbers. In order to do this, we made use of markers placed by the CT scanner on images saved in their original digital format on the CT computer.

The markers gave the exact CT number for the selected pixel, which were then compared to the result of applying our algorithm to that pixel. Figure 3.3 below shows how the markers were placed by the CT scanner.

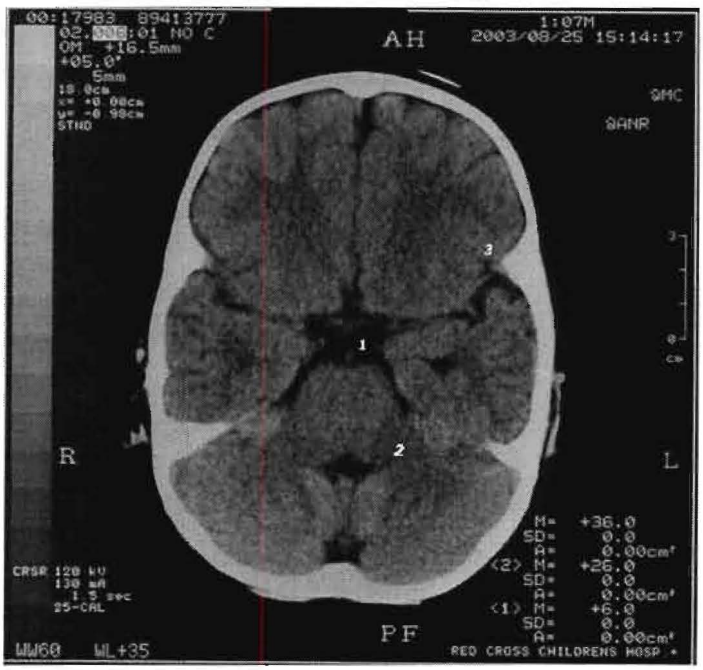

Figure 3.3 : Image showing the placed markers in white and the corresponding CT numbers in the bottom right of the image.

3.4.1 Method

1. 3 markers were placed on each of 14 different brain CT images that were stored in digital format at the Red Cross Children's Hospital. The markers were placed in various places in the brain and the CT numbers were displayed in the bottom right hand corner of the image. This image and a duplicate without the markers were printed to be used in the validation. The images were then scanned in order to recreate the conditions of the other images used in the project. Figure 3.3 shows the markers.

2. The placing of the markers on an individual pixel made it extremely difficult to identify the same pixel in the corresponding image that didn't contain the markers. To overcome this, the images with the markers and the one without, were registered in order to align them. The Matlab functions were used to register the images with an 'affine' transformation.

3. When registering the images, the first step involved loading both the images with markers and without, and using the *cpselect* function of Matlab in order to select corresponding pixels in both images. Selected manually at points corresponding in the images, eg: both images had writing on them, so making it easy to select a certain letter in both images. The greater the number of corresponding pixels selected, the greater the overall accuracy of the transformation. Matlabs *cpt2tform* function then used the selected pixels in order to generate a transform equation that would align the corresponding pixels. The *imtransform* equation was then applied to one of the images in order to align the total image, and therefore registering it with the other one.

4. Once the image were registered, it was possible to determine the co-ordinates of the pixel corresponding to the placed marker. This was done by using Matlabs *impixel* function which allows you to select manually the pixel of interest and then displays its co-ordinates. Once the correct pixel was ascertained, the CT number was reconstructed as described in section 3.3.5 Once this was complete the reconstructed number could be compared to the original placed by the CT machine.

3.4.2 Results of Quantitative Evaluation

In total 42 different pixels were evaluated. The results clearly indicated that the algorithm was effective in recreating the CT values, although errors were present which may be attributed to the factors discussed in 3.3.7.

Figure 3.4 below shows the comparison between the reconstructed values and the actual values

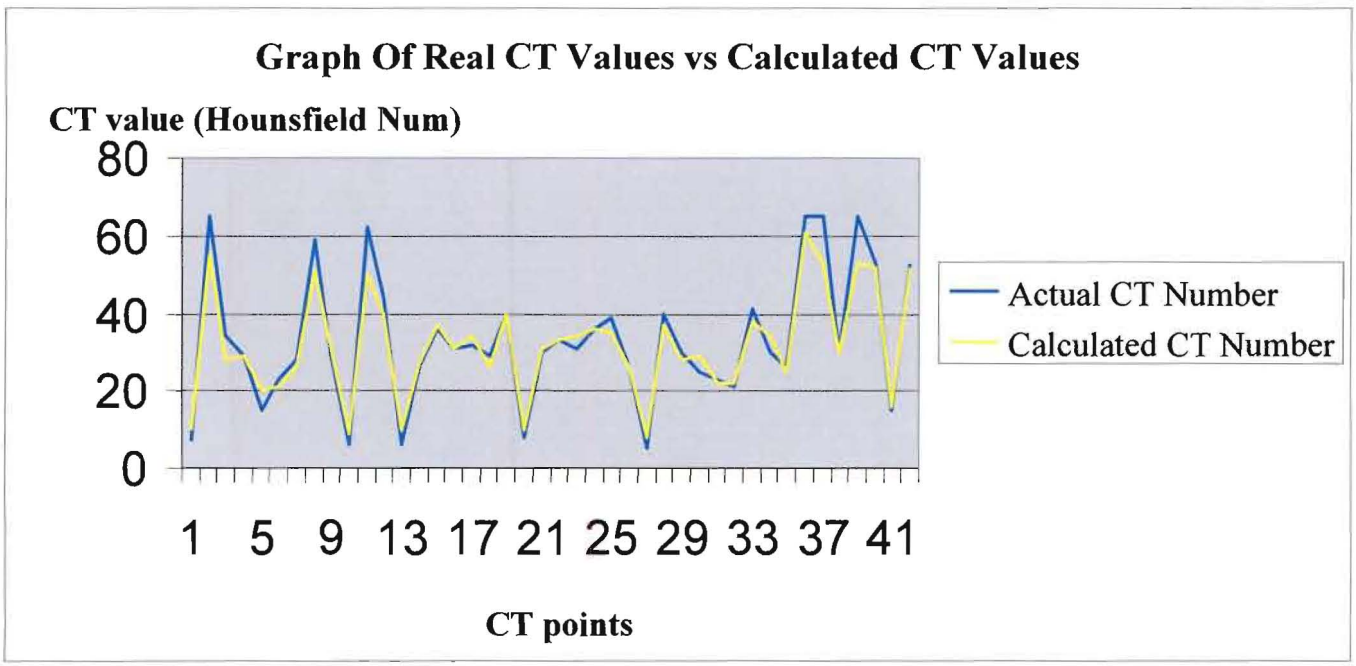

Figure 3.4: Graph showing the difference between the real CT value and the calculated CT value for all 42 pixels that were selected.

To verify that the error was not statistically relevant, a correlation test was run which produced a co-efficient of 0.98177 which indicates the familiarity of the data, and proves that the two sets of data are very similar.

In Table 1 below the vital information regarding the reconstructed and the original CT numbers are displayed.

Table Showing Various Measurements From The Reconstructed CT Values	
Measurement	**Difference between Actual & Reconstructed**
Max Value Difference	10
Min Value Difference	3
Mean Difference	1.2142
Std Deviation Difference	3.30076
Correlation	0.98177

Table 1: Table showing Statistics for the reconstructed CT numbers

The results above proved that the reconstruction algorithm described in section 3.3.5 may be used to obtain CT numbers from scanned hardcopy images. The full results from the validation can be found in appendix A.

3.5 Detection of hyperdensity

The CT films of all 17 patients with confirmed TBM, were scanned into softcopy using the method described in section 3.3.2. An experienced radiologist selected pixels in the scanned images that he suspected were hyperdense, and others that he regarded as normal. CT numbers of these pixels were reconstructed using the method described in section 3.3.5. For each of the 17 patients, the CT numbers confirmed that pixels identified by the radiologist as hyperdense, had higher CT numbers than those in the same image identified as being normal, as shown in Table 2.

Table of Expert selected hyperdense and normal pixels		
Image Numbers	**Hyperdense**	**Normal**
3_8	38.2	32.1
3_8	35.5	27.4
3_8	37.9	29.1
average	**37.2**	**29.5**
difference	**7.7**	
6_2	36.1	25.4
6_2	38.2	22.6
6_2	39	21.6
average	**37.8**	**23.2**
difference	**14.6**	
11_3	38.9	30.4
11_3	35.5	30.7
11_3	37.9	30.6
average	**37.4**	**30.6**
difference	**6.9**	
16_7	33.8	21.8
16_7	30.6	23
16_7	31.3	20.4
average	**31.9**	**21.7**
difference	**10.2**	
Average Difference	**9.8**	

Table 2: Showing The CT numbers of normal and hyperdense pixels identified by a radiologist

The column on the left of Table 2 shows 4 different images that were selected, and shows that 3 pixels were selected from each image, of both hyperdense and normal tissue. Three pixels were chosen in order to get an average density for each area. From the table it is clear that there was a large difference in most cases from the tissue that was thought be hyperdense compared with the normal tissue.

To allow for error, no pixels less than 5 Hounsfield units higher than normal were classified as hyperdense, but in most cases the hyperdense tissue was more than 5 higher than the normal tissue in the scan. The choice of 5 Hounsfield units was an estimate made by the expert

To better visualise the hyperdensity, the radiologist selected a CT number he felt was the upper limit of normal, and using thresholding, all pixels below this value were eliminated for a all 17 images. Figure 3.5 below shows an example of the thresholding.

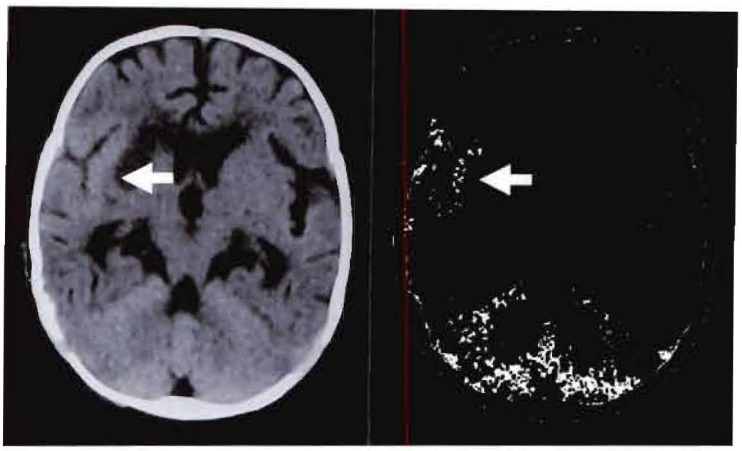

Figure 3.5: Image showing the original TBM image and the thresholded image on the right

Figure 3.5 shows a TBM image with the arrow pointing to an area deemed hyperdense by the radiologist. The image on the left has been thresholded in order to show the area of hyperdensity.

Figure 3.6 gives a further example of the thresholding and indicates an area of hyperdensity. The use of thresholding is unreliable as it is subjective and relies on the radiologits choice of cut-off CT number. Therefore a more independent and accurate way of visualising the hyperdensity was needed.

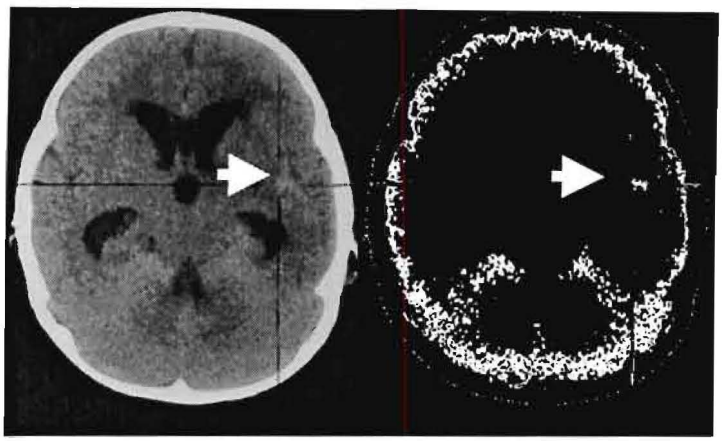

Figure 3.6: The image on the left shows an original TBM image, the image on the right shows the image after thresholding.

The results above proved that hyperdensity was associated with TBM, but in order to discount the possibility that hyperdensity may be present in normal CT scans, the same process was repeated on CT scans of 9 normal patients. The results showed that hyperdensity was not present in the normal CT and therefore can be classified as a sign associated with TBM.

From the 9 normal scans the radiologist was asked to identify the areas he thought had the highest density, measure those pixels and compare to an area he thought was normal.

Table 3 verifies our results of normal CT scans not containing hyperdensity. The CT numbers of the high density pixels were sometimes lower than the normals selected by the radiologist. The overall difference between the high density and normal pixels was only 0.1 which indicates that the normal CT scans do not contain hyperdense tissue.

Table of Expert selected pixels in normal scans		
	high density	Normal
notb2	36.9	32.8
notb2	34.2	31.9
notb2	31.9	30.8
average	**34.3**	**31.8**
difference	**2.5**	
notb3	35.8	38.3
notb3	35.6	29.7
notb3	36.9	39.4
average	**36.1**	**35.8**
difference	**0.3**	
notb4	31.1	31.7
notb4	35	32.5
notb4	26.7	31.9
average	**30.9**	**32.0**
difference	**-1.1**	
notb5	34.7	37.8
notb5	32.8	32.2
notb5	34.7	36.4
average	**34.1**	**35.5**
difference	**-1.4**	
notb6	30	34.4
notb6	34.7	33.1
notb6	38.1	31.7
average	**34.3**	**33.1**
difference	**1.2**	
Average Difference	**0.1**	

Table 3: Table showing the CT numbers of normal brain CT scans, where high density and normal pixels have been selected

3.6 Utility of quantitative evaluation of hyperdensity

Using the methods described in this chapter, radiologists were able to confirm that the areas they identified visually in CT scans of TBM children as being hyperdense, had abnormally high

4 FUZZY CLUSTERING

Pattern recognition to extract desired data from a data set is a widely researched area and is applied in fields ranging from business to medicine. As computers have increased in capacity and speed, pattern recognition has become more useful as now users have the ability to search for patterns in very large data sets.

Imaging is invaluable in medical diagnosis due to its non-invasive diagnostic capabilities. At present the medical imaging field is highly dependant on human pattern recognition, with radiologists being highly trained to search for patterns in images from all modalities. Computers have an important role in aiding radiologists in pattern recognition, by speeding up their work rate, while reducing the work load.

The various types of pattern recognition algorithms lend themselves to different applications. In this project the goal was to identify a pattern that consists of hyperdense tissue. The most obvious and simple technique would therefore lie in segmenting the images into different tissue types, one of which should be the hyperdense tissue.

The majority of research on the segmentation of structural brain images is done on MRI, and few algorithms have been developed for use with CT images. As CT images have poorer image quality than MRI, the algorithms used in MRI may not be appropriate when applied to CT. The fundamental problems with CT are the uncertainty in the data and the noise introduced by the CT machine.

Cosic and Loncaric (1996) have presented the only CT specific algorithm for segmenting brain images. In the study, they segmented head CT images, in order to extract intracerebral brain haemorrhage. The haemorrhage presents as very high density tissue, approximating the density of bone, and was therefore easily segmented using a fuzzy clustering algorithm based on the work of Gath and Geva (1989).

of bone, and was therefore easily segmented using a fuzzy clustering algorithm based on the work of Gath and Geva (1989).

Although used in a different context, the algorithm is suitable for this project, as it was also used to segment tissue of a higher density than that of normal tissue. It combines both statistical and fuzzy methods, thus overcoming some of the problems, such as uncertainty, associated with CT images.

By using various methods of pre-processing in order to increase the image contrast followed by applying the fuzzy maximum likelihood estimation algorithm we segmented our 17 TBM images into various tissues. Further clustering then resulted in a hyperdense region being segmented for each image.

4.1 Image Selection

Up to 16 CT slices were available for each patient. From the set of images of TBM patients, an expert radiologist selected for 17 patients, one image that he judged to contain the most obvious hyperdensity.

12 cases were selected by the expert radiologist and the final 5 of the 17 cases were selected without expert opinion in order to compare the results. They were selected by a non expert, who was instructed to choose an image he thought may have brain tissue that appeared lighter in colour than the surrounding brain matter. The choice was made from only those images that could possibly highlight TBM. This meant that image slices that were too low anatomically and showed the orbital structures were eliminated from his choice.

Once all 17 patients had 1 or 2 images associated with them, these images were ready to be used in the study. Images of 9 patients with normal scans were selected at random from a patient base. One image was selected from each patients set of scans, at a level where hyperdensity might have been detected in a TBM patient.

4.2 Image pre-processing

In order to reduce computational time extraneous information needed to be eliminated before the program was run. This was achieved by the simple procedure of cropping the images to a standard size in order to eliminate the writing placed in each image. Figure 4.1 shows the result of cropping the images.

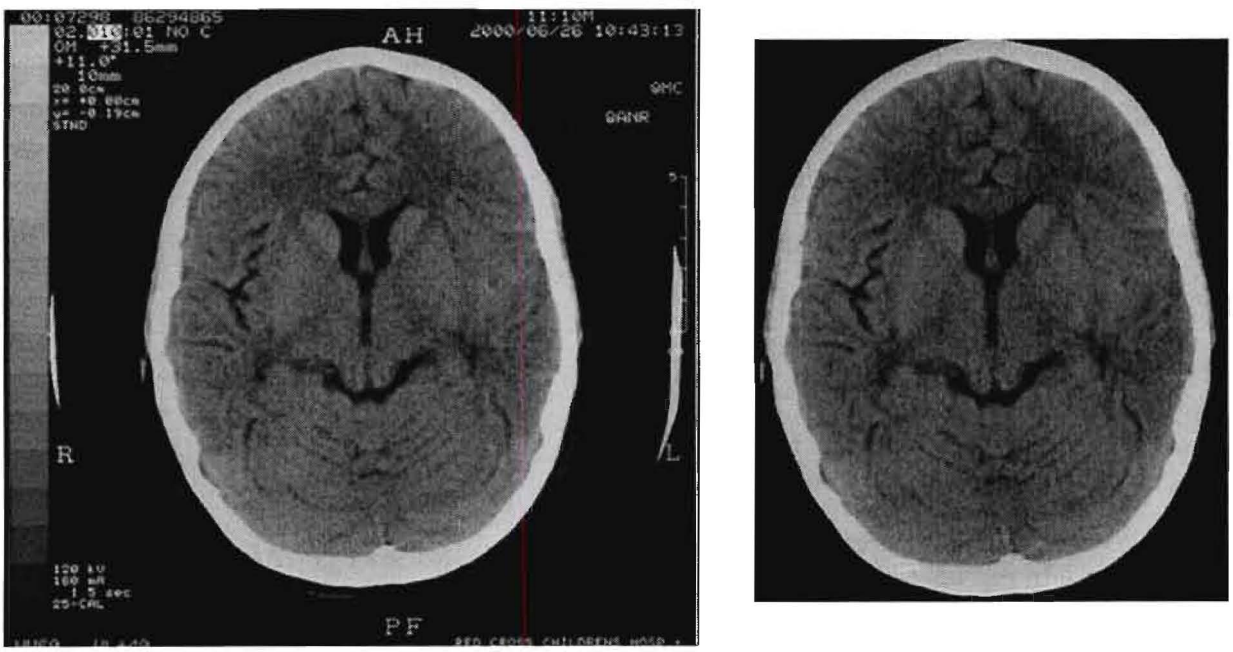

Figure 4.1: The image on the left shows the original image. The image on the right has been cropped in order to eliminate unnecessary information and reduce the size.

4.2.1 Image Enhancement by contrast stretching

The algorithms discussed above provide good clustering results. In order to improve these, we made use of an image enhancement technique before the images underwent the clustering. The

image enhancement improved contrast so that the input images to the algorithm were easier to segment and would cluster faster.

Each image in Matlab contains a colour map. This specifies the colours used in an image, and in order for the best contrast, the colours need to be clipped at certain intensities. Matlab has a built in function called *stretchlim* that finds the intensities in an image that will provide the most contrast. The image is then mapped to the range specified by *stretchlim* and so provides maximum contrast. Figure 4.2 below shows the results of contrast stretching.

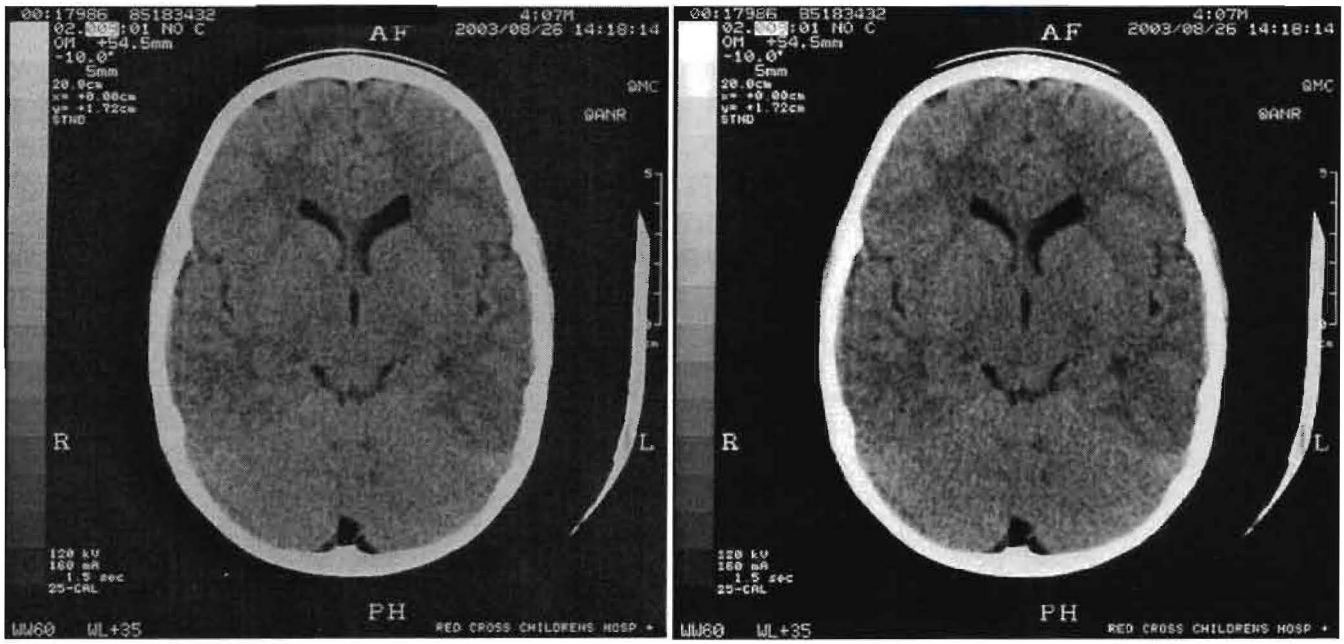

Figure 4.2: Showing 2 normal head CT images. The image on the right has undergone contrast stretching

The images in Figure 4.2 clearly show that the image on the right has better contrast than the original and therefore would be easier and faster to segment.

4.3 Clustering Algorithm

4.3.1 Comparison of K-means and Fuzzy C-Means Algorithms

K-means clustering is the simplest from of clustering and was discussed in section 2.8. It is simple to implement and requires little computational time.

The fuzzy c-means algorithm was explained in section 2.10. The use of fuzzy logic made the algorithm more suitable to the image data used in this project than conventional k-means clustering, as imprecision in the data was better represented. The imprecision in the data is caused by noise, which can change the CT value of the pixel and can be better handled by a fuzzy algorithm that accounts for uncertainty in data.

In Figure 4.3, the image on the left is a normal CT brain scan that has been segmented into 4 different clusters using k-means clustering. The 4 clusters were intended to represent white matter, grey matter, skull and ventricles. The image on the right is the same original image after being segmented using fuzzy c-means clustering also with 4 clusters. The fuzzy c-means image gives a better approximation of grey matter in the brain than the k-means where some grey matter has been misclassified as white matter (see the red arrows).

The value of q used in the fuzzy c-means was 2. This value was chosen as it has good correlation with the literature and is computationally easier to implement (Gath and Geva, 1989).

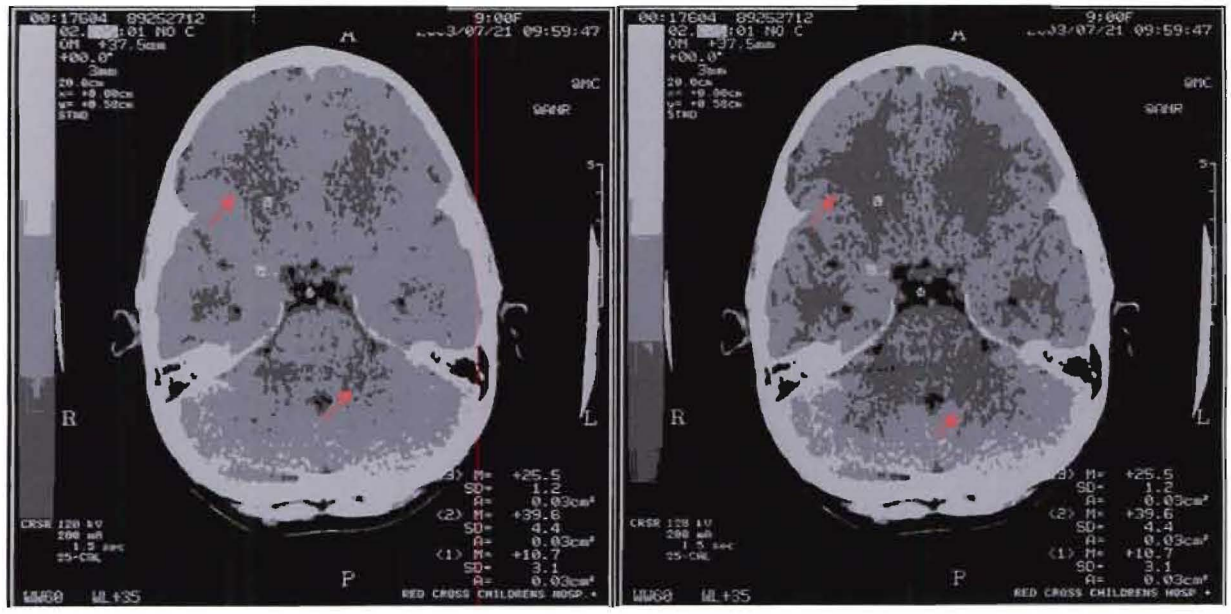

Figure 4.3: Showing two brain CT images that have been segmented using k-means clustering and fuzzy c-means clustering respectively

Figure 4.4 Shows an MRI that is taken at approximately the level of the lateral ventricle which is similar to Figure 4.3. The MRI better identifies the grey and white matter and shows the superiority of image quality over CT. It shows how the k-means clustering has confused white matter as skull when looking at the skull cluster in Figure 4.5 (The red arrows mark white matter that has been classified as skull).

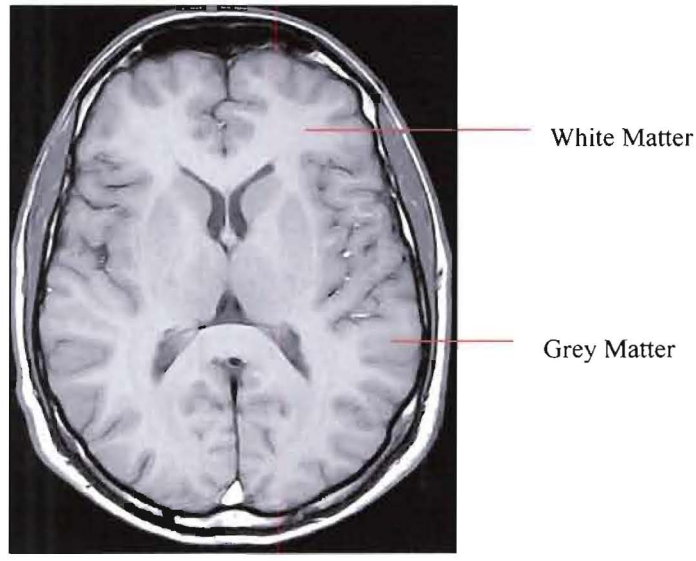

Figure 4.4: MRI image of a normal brain

In Figure 4.5, the image at the top left is the original image that k-means clustering was applied to. The number of clusters was set to 3, with the anticipated 3 clusters corresponding to brain, skull and ventricles.

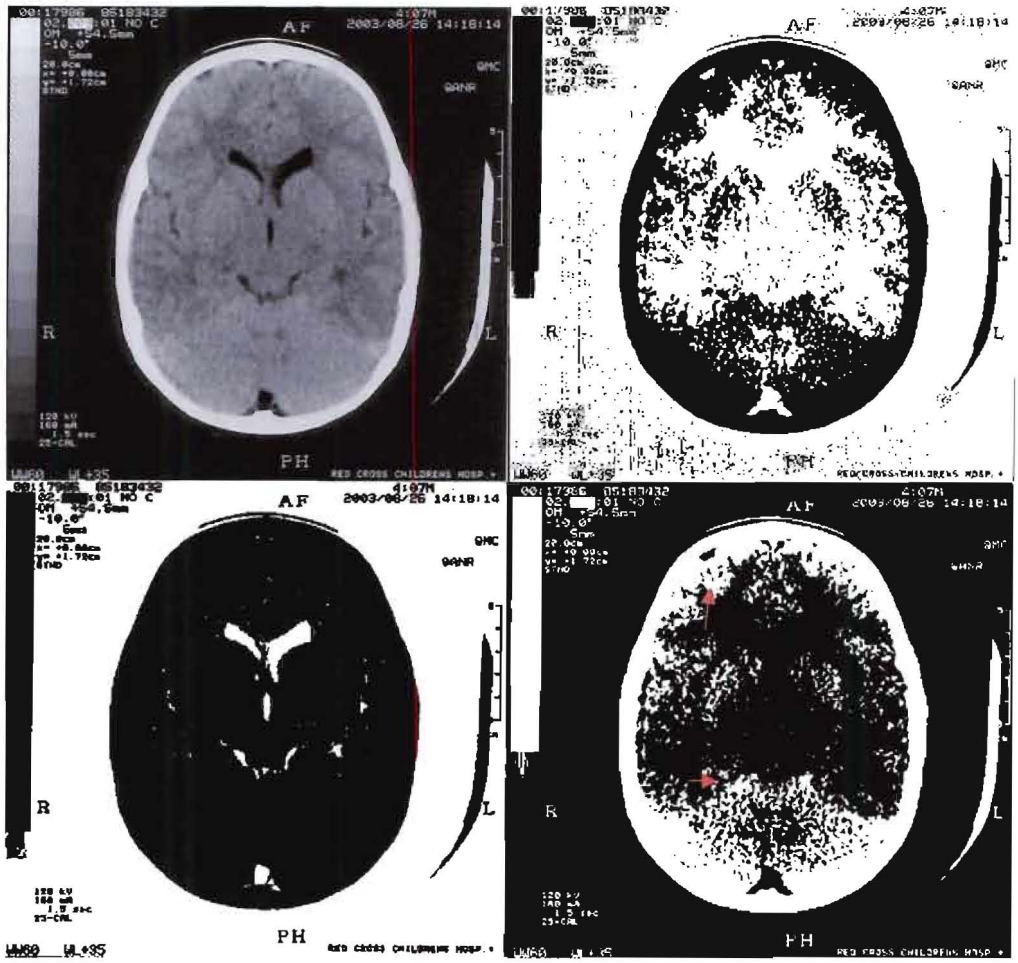

Figure 4.5: Images showing the results of applying k-means clustering to a normal brain CT scan

The image at the top right is the cluster representing the brain. It is clear that the brain region has not been accurately segmented, and when compared to the image at the bottom right – the skull region, it is clear that many pixels have been misclassified for both regions.

The image in the bottom left represents the best clustering and is the ventricle region. Due to the high contrast between the brain tissue and the black ventricles, it was also the easiest to segment correctly.

Figure 4.6 below shows the superiority of fuzzy c-means clustering over that of k-means. The fuzzy c-means algorithm was applied to the same image as in Figure 4.5. When comparing the brain regions it is clear that FCM has misclassified fewer pixels than the k-means, and the same applies to the skull regions. When comparing the ventricle regions the differences are less clear and more comparable.

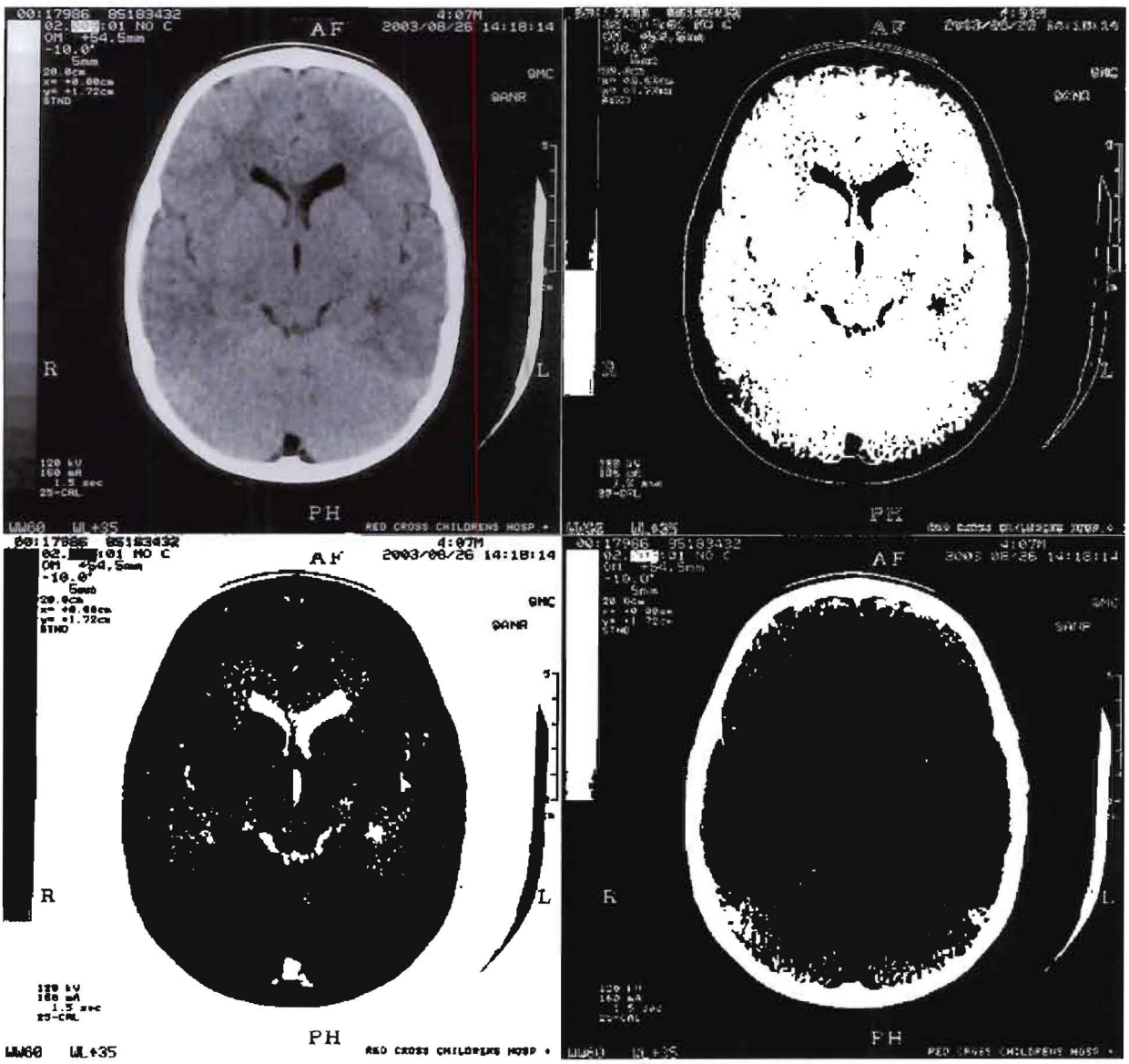

Figure 4.6 : Images showing the results of applying fuzzy c-means clustering to a normal brain CT scan

The fuzzy c-means algorithm makes use of a Euclidean distance measure in the error criterion. Although this is effective for most cluster shapes, it is not the optimal distance measure for clusters with variability in their shapes and densities and also for varying number of data points in each subset. Gustafson *et al* (1979) compared several fuzzy clustering algorithms used to segment data with variable cluster shape and overlap of the clusters. The study found that the normal fuzzy c-means failed to account for class shape and tended to impose spherical clustering shapes due to the distance measure. The study tested the use of the fuzzy covariance matrix as a distance measure and found it to be superior to the Euclidian distance.

For clusters with variable cluster shapes and densities, a new exponential distance measure which is combined with the fuzzy covariance matrix gives better clustering results and is therefore superior in clustering to the fuzzy c-means algorithm (Gath and Geva, 1989). This algorithm, the fuzzy maximum likelihood estimation (FMLE) is discussed in section 4.3.2.

The ease of implementation of the fuzzy c-means makes it a popular algorithm for most cases of clustering. It has a relatively fast run time, and the good preliminary results made it a suitable starting algorithm for use in this project.

4.3.2 Fuzzy Maximum Likelihood Estimation (FMLE)

The research has shown a number of possible new techniques such as neural networks and genetic algorithms to overcome the sensitivity of the fuzzy c-means algorithm to different cluster shapes. The problem with these types of algorithms is the difficulty in implementation and the long processing time. These algorithms are also sensitive to noise. Statistical methods combined with the fuzzy clustering are well established and yield comparable results to neural networks and genetic algorithms, with a large saving in time and ease of implementation (Lawrence *et al,* 1992).

The difference between the traditional statistical clustering methods and FMLE is the use of fuzzy logic in the algorithm, thus making it better suited to applications containing uncertainty in the data.

The biggest difference between the fuzzy statistical and the fuzzy c-means methods is the distance measure rather than the statistics. The distance measure in the former case is an exponential one. The use of the exponential measure makes the algorithm more robust to the problems of various cluster shapes, cluster densities and differing numbers of pixels in each cluster by being able to account for account for different pattern shapes in the data (Gath and Geva, 1989). This measure therefore gives better segmentation of the images and more accurate clustering.

The statistical method introduced is maximum likelihood estimation (MLE). Maximum likelihood estimation begins with a mathematical expression known as the Likelihood Function of the sample data (which in this case is the image pixels). The likelihood of a set of data is the probability of obtaining that particular set of data, given the chosen probability distribution model. This expression contains unknown model parameters. The values of these parameters that maximize the likelihood of the sample data are known as the Maximum Likelihood Estimates or MLE's (NIST/SEMATECH, 2004).

A limitation of the algorithm is also the solution to the optimal clustering, namely the exponential distance, which forces the algorithm to search for an optimum solution in a very narrow local region. This means that the algorithm can become unstable if it doesn't start from 'good' cluster prototypes (Gath and Geva, 1989).

4.3.3 Implementation of the FMLE Algorithm

The FMLE algorithm follows much the same sequence as the fuzzy c-means algorithm. The steps taken to implement the algorithm follow below, and is based on the algorithm by Gath and Geva (1989):

1. Choose initial cluster centres
2. Calculate the posterior probability (the probability of selecting the *i*th cluster given the *j*th feature vector) $h(i|X_j)$

$$h(i|X_j) = \frac{1/d_e^2(X_j, V_i)}{\sum_{k=1}^{K} 1/d_e^2(X_j, V_i)} \qquad (2)$$

Where X_j is the *j*th feature vector, V_i is the centroid of the *i*th cluster and K is the number of clusters.

$$d^2{}_e(X_j, V_i) = \frac{[\det(F_i)^{1/2}]}{P_i} \exp[(X_j - V_i)^T F_i^{-1}(X_j - V_i)/2 \qquad (3)$$

Where F_i is the fuzzy covariance matrix of the *i*th cluster, and P_i is the *a priori* probability of selecting the *i*th cluster.

3. Step 3 involves 3 equations, firstly computing new centroids from

$$\hat{V}_i = \frac{\sum_{j=1}^{N} \left(h(i|X_j)\right)^q X_j}{\sum_{j=1}^{N} \left(h(i|X_j)\right)^q} \qquad (4)$$

Once the new centroids have been calculated the next equation is the *a priori* probability of selecting the *i*th cluster.

$$P_i = \frac{1}{N}\sum_{j=1}^{N} h(i|X_j) \qquad (5)$$

Lastly the fuzzy covariance matrix must be calculated from:

$$F_i = \frac{\sum_{j=1}^{N} h(i|X_j)(X_j - V_i)(X_j - V_i)^T}{\sum_{j=1}^{N} h(i|X_j)} \qquad (6)$$

4. Finally calculate the error criterion - ϵ ,which lies between 0 and 1

$$\max \left| h(i|X_j) - \hat{h}(i|X_j) \right| < \epsilon, \qquad (7)$$

5. If the error criterion is satisfied, in this case it has been set to 0.05, then stop, otherwise repeat the algorithm until the error converges to within the range.

When the algorithm ends, it means that the new posterior probability that is calculated in each cycle is changing by less than 0.05 which will make very little difference to assigning pixels to different clusters. The iterative processes of the algorithm results in the convergence of the cluster centroids to a local optimum, indicating the best possible segmentation has been achieved.

Several of the variables calculated above rely on previous information. In step 2, the calculation of the posterior probability depends on calculation of the exponential distance, which in turn relies on calculation of the fuzzy covariance matrix and the *a priori* probability, which are only calculated at a later stage. What this implies is that the algorithm needs some prior knowledge or that the user should choose initial variables.

As the algorithm searches for an optimal solution in a narrow region, initialisation of the variables at values close to their optimal values is necessary. A simple answer is to run the fuzzy c-means algorithm first and use the variables from it to initialize the FMLE.

The fuzzy membership u_{ij} was obtained from the FCM algorithm and this was replaced by the posterior probability $h(i|X_j)$ in the FMLE algorithm. This was done because when the variable q is set to 2, such as it is in this case, the two terms are equivalent, except for the type of distance measure used.

The fuzzy covariance matrix was calculated for each of the clusters identified by the FCM algorithm and used to initialize the new distance equation. Finally the initial *a priori* probability was calculated from equation (5) by substituting u_{ij} for $h(i|X_j)$.

These initial starting variables were successful in initiating the FMLE and didn't have to rely on 'guesses' from the programmer which would have increased calculation time dramatically. The starting clusters which have already been fairly well classified, provide the FMLE algorithm with initial cluster centres, allowing it to concentrate on further clustering without the possibility of the algorithm becoming unstable and failing to segment properly.

The combined algorithm would be expected to give more accurate clustering than the FCM algorithm. Unfortunately the use of two algorithms doubles the processing time, and the higher the number of clusters that the image is segmented into, the higher the execution time. Eliminating extraneous information as described in section 4.2 is therefore important.

The combined algorithm, although time consuming, gave much better clustering results than simple FCM. A few examples follow below in Figure 4.7.

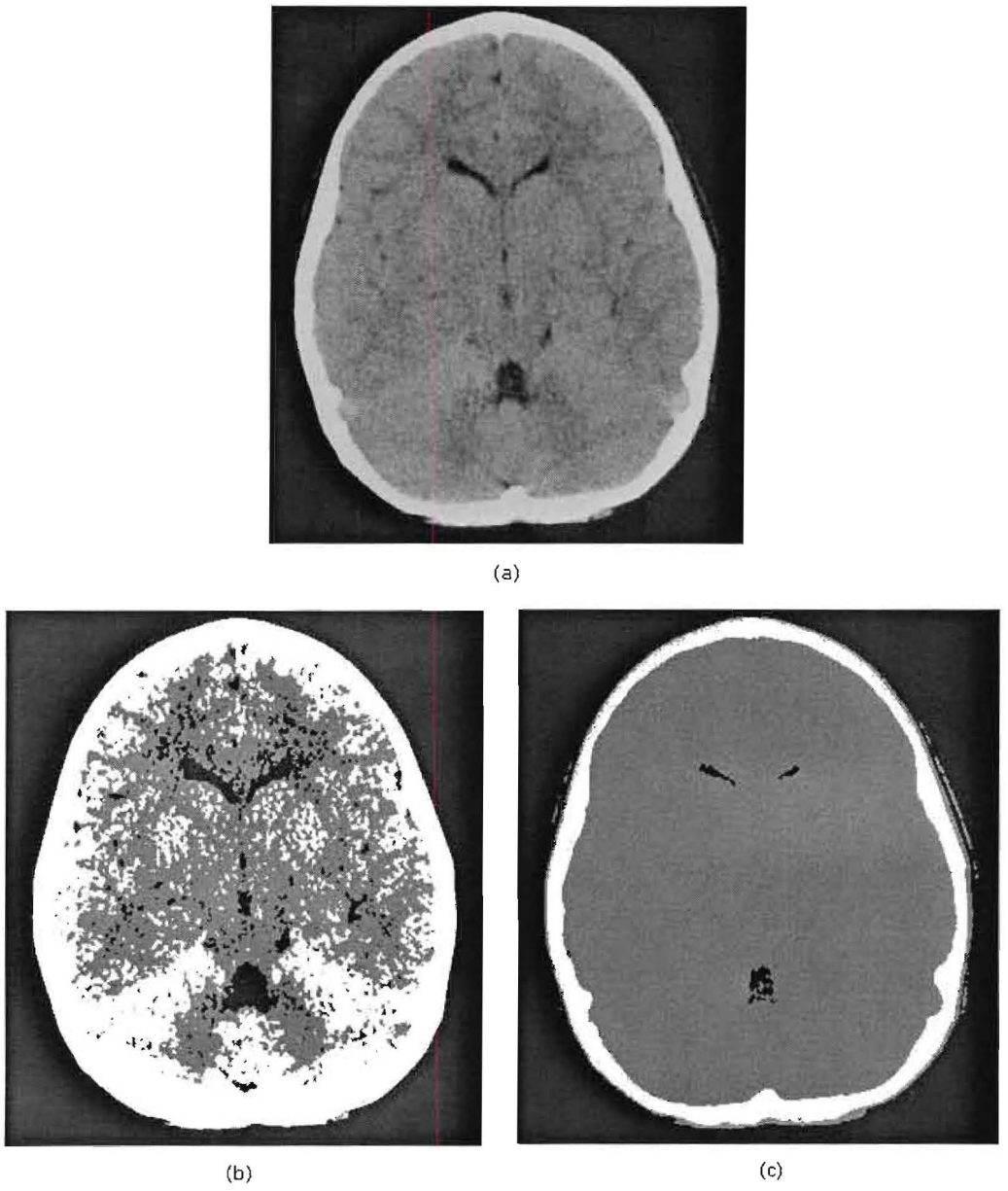

Figure 4.7: Images showing the comparative results of applying an FCM algorithm and a FMLE algorithm (a) shows the original brain CT image of a patient with a normal brain scan. In image (b) the scan has been segmented using fuzzy c-means clustering into 3 clusters, and image (c) has been segmented using the Fuzzy maximum likelihood estimation (FMLE) into 3 clusters.

As can be seen from the images in Figure 4.7 it is evident that the FMLE does a better job than FCM at clustering the images. Both images have been segmented into 3 clusters, Brain, Skull and Ventricle. The FCM has misclassified many of the brain pixels as skull and vice versa,

whereas the FMLE seems to give a clearly delineated brain, skull and ventricles when compared to the original image.

To further highlight the differences, it is valuable to look at the clusters separately so that a better comparison can be made. The images that follow are the 3 separate clusters that made up the images in Figure 4.7 (b) and (c).

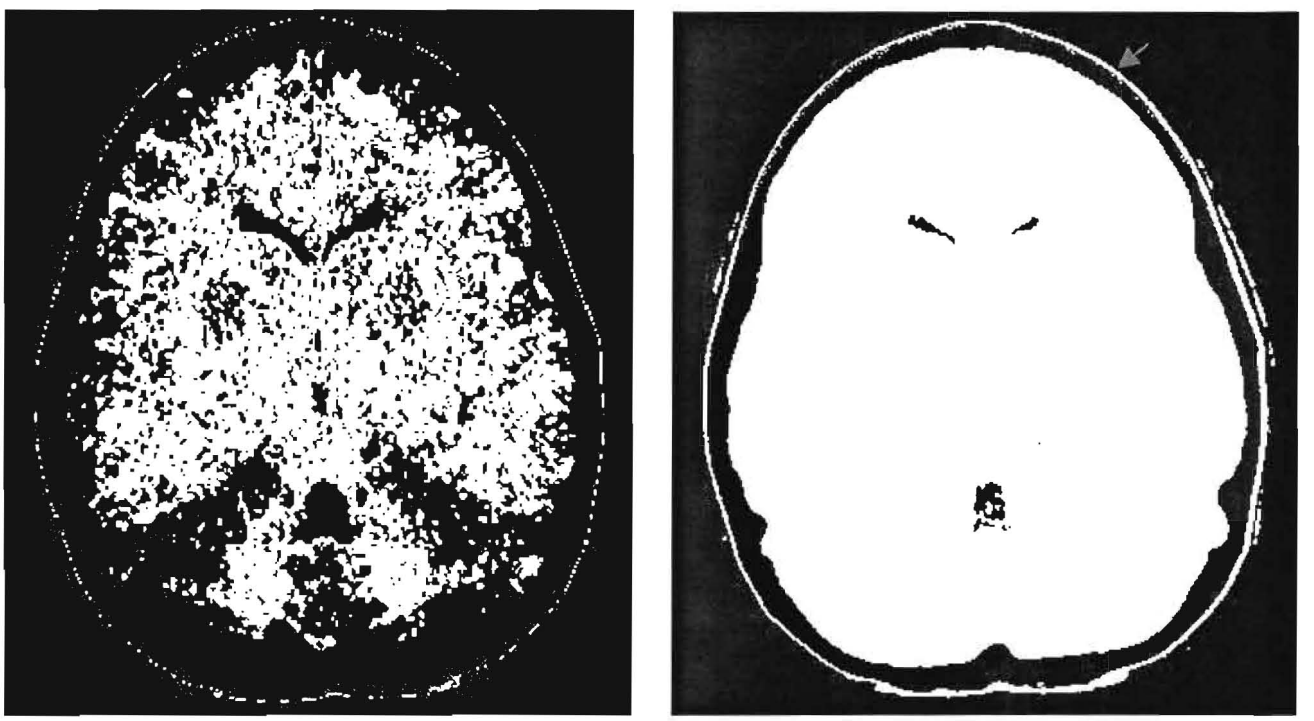

Figure 4.8: The image on the left shows the brain cluster segmented using FCM. The image on the right shows the brain cluster segmented using FMLE.

Figure 4.8 shows the separate clusters from the images in Figure 4.7 (b) and (c). Here the large discrepancy between the clustering results is evident. The very scattered appearance of the brain in FCM segmented image indicates a number of pixels have been wrongly allocated, where as the FMLE segmented brain cluster is smooth and continuous. The outline around where the skull would have been (red arrow) is caused by uncertainty in the image, which was discussed in section 2.7

The sharp boundary between skull and air, is associated with uncertainty and when the image is digitised it results in an outline around the skull of tissue that can be classified as brain matter.

Figure 4.9 contains the separated ventricle clusters from figure 19 (b) and (c) compares them to one another.

Figure 4.9: Shows two images of the ventricle cluster from segmentation of normal brain CT scan. The image on the left has been segmented using FCM and the image on the right with FMLE.

The FCM segment shows clear signs of misclassification; many of the pixels that should be associated with the brain cluster have been included in this ventricle cluster. The FMLE cluster has clearly segmented only the ventricles, making it possible to perform measurement of the ventricles for other purposes.

The final cluster - Figure 4.10, is that of the skull, and shows the best example of why FMLE is superior to FCM.

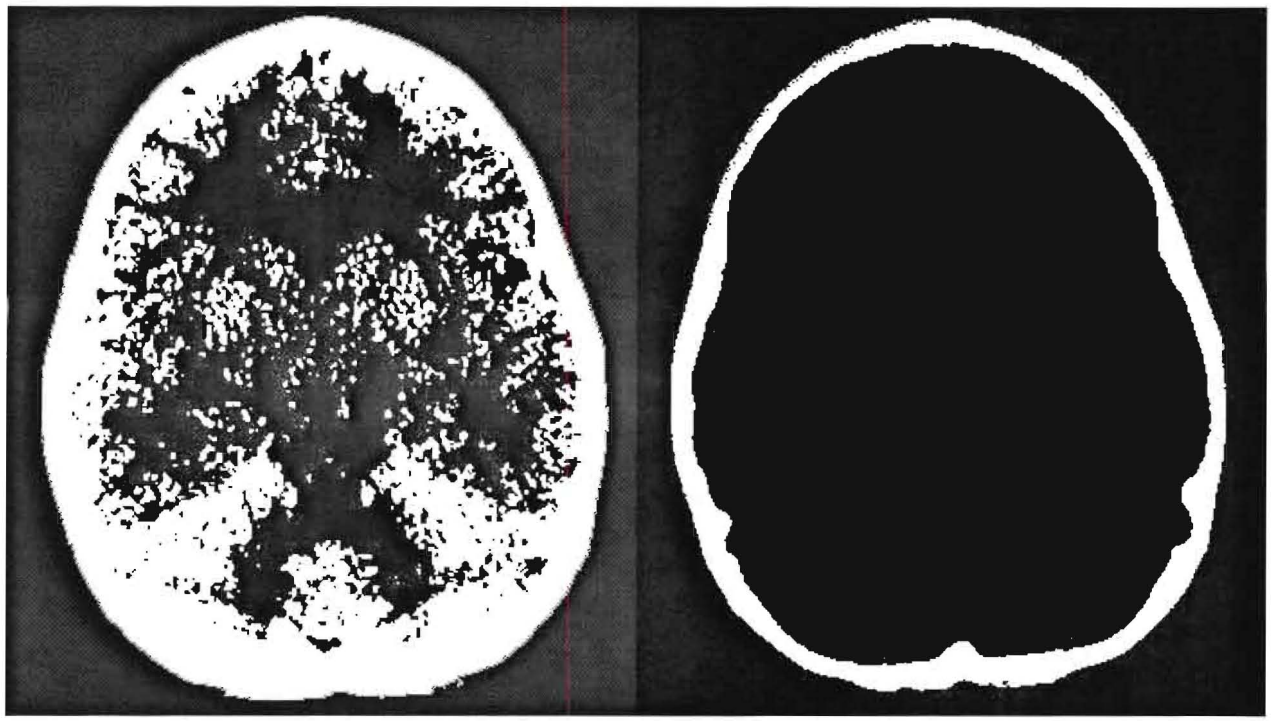

Figure 4.10: The images show the skull clusters resulting from segmenting a normal brain CT scan. The image on the left has been segmented using FCM and the one on the right with FMLE.

These images provide the biggest difference between FCM and FMLE. The FCM cluster includes large portions of brain pixels in the images, where as the FMLE has a perfect, clearly defined skull region.

The superiority in clustering of the FMLE has the price that the execution time is more than double that of FCM. In the context of this project, execution time is not highly critical, therefore we choose FMLE for its superior clustering, remembering that FCM is incorporated in the FMLE algorithm. FMLE may not be suitable for real-time implementation due to the time concerns.

4.3.4 Autonomous Cluster Selection

One of the biggest limitations of clustering techniques is their reliance on prior knowledge. The algorithm described in section 4.3.2 relied on the prior knowledge of how many clusters to use.

This is undesirable as not all images are the same, and the number of clusters should not be a set variable before the algorithm is executed.

Depending on the contrast in images, the number of optimal clusters can be very different. For example in an image that has high contrast between the grey and white brain matter, it would be more desirable to segment the brain image into 4 clusters instead of the previous examples of 3 clusters in order to separate grey and white matter. Ideally criteria should exist for the algorithm to decide on the optimal number of clusters to include.

In order to make the algorithm unsupervised, that is, no input or prior knowledge about the data set is needed for the algorithm to function properly, a system of performance measures was developed in order to guide the algorithm during the segmentation.

The goal of the measures was defined to be that of obtaining 'good' clusters. The measures could then be based on the effectiveness of the cluster versus the number of clusters. Defining what is meant by a 'good' cluster is a difficult task. Gath and Geva (1989) chose an approach based on minimizing the classification error rate, and our project tackled the problem in the same way.

The definition of optimal partitions includes 3 requirements:

1) Clear separation between the resulting clusters
2) Minimal volume of the clusters
3) Maximal number of data points concentrated in the vicinity of the cluster centroid

The first requirement of clear separation between the clusters, simply means that data must be well clustered, so as not to have overlapping of the clusters. While the algorithm relies on fuzzy logic, well defined subgroups are desired, which in turn will lead to a harder partitioning of the data. This means that although the mechanism is fuzzy, the aim of the classification is the generation of well-defined subgroups.

By minimising the volume of the cluster, all the pixels in the cluster would be closely packed together and therefore have a high fuzzy membership to that cluster. If the pixels were further away from the cluster centre the volume would be larger, and the pixels would have an increased fuzzy membership to other clusters.

Having the maximum number of pixels close to the centroid of a cluster, means that the cluster centre value is strongly associated with a particular group of pixels.

The performance measures used in this project were fuzzy hypervolume and partition density (Gath and Geva, 1989). They address all 3 requirements mentioned above. The hypervolume is responsible for minimizing the volume of the clusters, and the partition density ensures that the maximum number of data points is concentrated near the cluster centroid. Both ensure clear separation between clusters.

4.3.5 Performance Measure Algorithm

The first equation in the algorithm gives the fuzzy hypervolume, represented by F_{HV} and is defined as:

$$F_{HV} = \sum_{i=1}^{K} [\det(F_i)]^{1/2} \qquad (8)$$

Where F_i is the fuzzy covariance matrix and is calculated from equation (6)

The average partition density D_{PA} is calculated from

$$D_{PA} = \frac{1}{K} \sum_{i=1}^{K} \frac{S_i}{[\det(F_i)]^{1/2}}$$

The average partition density is not used in the equations, but is described due to its' importance in the understanding of how partition density is calculated.

Where S_i is the sum of central members and is given by the equation

$$S_i = \sum_{j=1}^{N} u_{ij}$$

To calculate the partition density P_D, we take into account only the members within the hyperellipsoid , whose radii are the standard deviation of the cluster features.

$$P_D = \frac{S}{F_{HV}} \qquad (9)$$

where

$$S = \sum_{i=1}^{K} \sum_{j=1}^{N} u_{ij}$$

Equation (8) and (9) are applied to the data in order to calculate performance and the number of clusters for segmentation can be obtained from the results of these equations.

Our requirements for a 'good' cluster are that there is a maximum number of data points concentrated near the cluster centroids. Partition density gives us a numerical way of evaluating this concentration of data points. Figure 4.11 shows the graph of the partition densities for different numbers of clusters. The highest density is present when there is only one cluster, but obviously this is an unrealistic case for segmenting an image. The next maximum of partition density occurs for 3 clusters, and then continues to decline for increasing numbers of clusters.

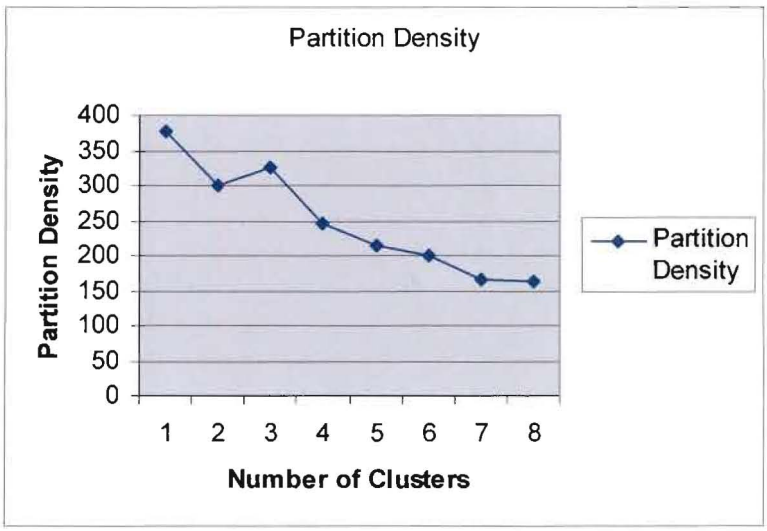

Figure 4.11 : Graph showing an example of the partition density measure obtained from FMLE of a CT scan of a TBM patient. The graph shows the partition density versus the number of clusters.

This maximum partition density for 3 clusters is a good starting point for performance measurements, but the volume of the clusters must still be taken into account: hence we compute the fuzzy hypervolume and again illustrate using a graph.

When considering volume, pixels in a cluster should occupy the smallest volume to indicate a tightly packed cluster, meaning effective clustering. Figure 4.12 shows the hypervolume values for different numbers of clusters. The minimum in this case occurs when the image is segmented into 3 clusters.

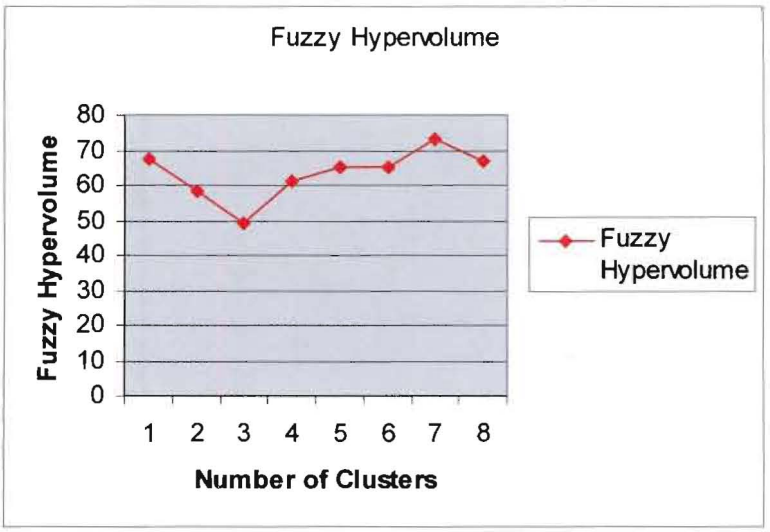

Figure 4.12: Graph showing an example of fuzzy hypervolume versus number of clusters obtained from a CT scan of a TBM patient using FMLE.

Now that partition density and fuzzy hypervolume both confirm that for optimal clustering, the image should be segmented into 3 clusters, we can clearly see how these measurements provide parameters for decision making in the algorithm.

For this example 3 clusters provide the best clustering as we have defined it. The number of optimal clusters may differ from image to image, therefore the performance measures must be calculated for each new image that is clustered.

The clustering process starts with 2 clusters – the minimum number of starting clusters. After the error criterion for clustering has been reached, the performance measures are calculated. If they do not satisfy the criterion of being the minimum hypervolume and the maximum hyperdensity, another cluster must be introduced and the algorithm is now repeated for 3 clusters. When the minimum hypervolume and maximum partition density are found, the algorithm is satisfied that the best possible partitioning of the data has been found.

When the performance measures are being calculated, the previous hypervolume and partition density are compared to the newly calculated ones. If the hypervolume is higher than the previous one, it is likely that the minimum value was found on the previous iteration. Similarly

if the current partition density is then lower than the previous one, the algorithm can conclude that the maximum partition density and the minimum hypervolume were found on the previous iteration and the algorithm is stopped.

4.3.6 New Cluster Placement

If the performance measure calculations have indicated the need for more clusters to be added to the current clustering process, a decision must be made as to where best to place this new cluster. Important factors to consider when deciding on the placement are that incorrect placement may result in extended processing time, or possible instability in the algorithm.

The main requirement when choosing a new cluster centre is to place it in an area where the fuzzy membership values to the other clusters are low. This means that the pixels in this area are not strongly associated with the clusters that are already there. If the cluster is placed in an area which has high fuzzy membership to the existing clusters, the clustering algorithm will have a problem allocating the pixels to the new clusters. The algorithm must then actually move the cluster centre through the iterative process to a place where the fuzzy membership is low. This would mean that execution time is largely increased, which is not desirable in a process that already has a long execution time.

A study by Cosic and Loncaric (1996) compared 3 different methods for placing new clusters in unsupervised fuzzy clustering applied to CT head images. The clustering algorithm used was very similar to the one used in this project and was based on the (Gath and Geva, 1989) algorithm with the only change being the selection of the new cluster. The results of the study which computed the cluster validity and speed of convergence revealed that one method of placing a new cluster was superior. The cluster validity used was the same as the performance measures used in this project to calculate whether a new cluster needed to be added. The speed of convergence was the time it took for the clustering to be completed.

Our project utilised pre-processing and the same algorithm used by Gath and Geva (1989), with the inclusion of one of the cluster selection methods discussed by Cosic and Lonacric (1996).

The method that proved the fastest also gave slightly better head segmentation results and therefore was chosen to be used in this project. The following equation that was used:

$$p = \arg\min_j \max_i u_{ij}, \quad V_{K+1} = X_p \qquad (10)$$

Where u_{ij} is the fuzzy membership to each cluster, i is the cluster number, and j is the pixel co-ordinates. V_{K+1} is the new Cluster to be added, and X_p is the pixel intensity of the pixel whose co-ordinates are specified by p.

Equation 10 selects the pixel value that must be used as the new cluster starting point. The equation first seeks the i value that maximizes u_{ij}. Then the equation searches for the j value that minimizes u_{ij}. The algorithm then selects the cluster specified in i and then finds the pixel represented by j in that cluster and this pixel gives the value where the new cluster must be placed.

Including performance measures and a way of calculating the placement of a new cluster, result in an unsupervised clustering algorithm. This means that it is autonomous and does not rely on the user for input other than the images. This eliminates the need for prior knowledge and also reduces the amount of technical expertise the user of the program requires.

4.4 Clustering Solution

The final algorithm consists of many components which all combine together to provide an effective clustering solution. A description of the final algorithm follows below:

1) Apply the pre-processing to increase contrast in the images

2) Cluster the image with Fuzzy c-means clustering (FCM), starting with two initial clusters and using unsupervised clustering

3) Cluster the image using the fuzzy modification of the maximum likelihood estimation (FMLE). (Gath and Geva, 1989)

4) Compute the performance measures. (Gath and Geva, 1989)

5) Compute new cluster position and add new cluster prototype.(Cosic and Loncaric, 1996)

6) Repeat steps 1- 3 until the performance measures are satisfied

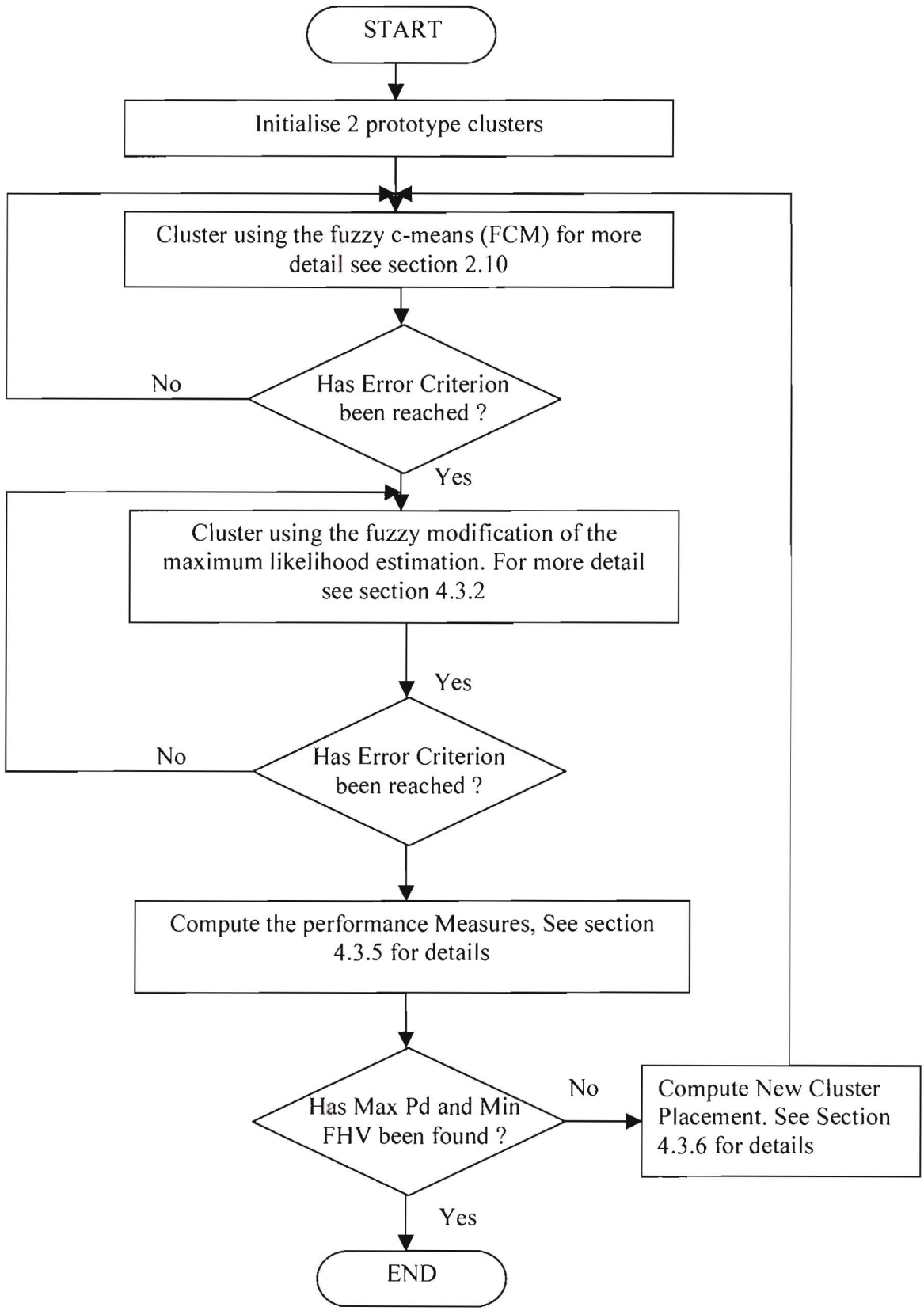
START
Initialise 2 prototype clusters
Cluster using the fuzzy c-means (FCM) for more detail see section 2.10
No
Has Error Criterion been reached ?
Yes
Cluster using the fuzzy modification of the maximum likelihood estimation. For more detail see section 4.3.2
Yes
No
Has Error Criterion been reached ?
Compute the performance Measures, See section 4.3.5 for details
Has Max Pd and Min FHV been found ?
No
Compute New Cluster Placement. See Section 4.3.6 for details
Yes
END

4.4.1 Comparison of FCM, FMLE and new algorithm

The two fuzzy algorithms applied in this project, are the fuzzy c-means and the fuzzy modification of the maximum likelihood estimation. Although these two algorithms are combined to form the optimal clustering algorithm described above, they are stand alone algorithms in their own right and have been used in clustering for many years.

The fastest in terms of execution time is FCM, but also the least accurate. The FMLE gives good clusters, but relies on prior information to remain stable. The combined algorithm which we have named the 'unsupervised optimal fuzzy clustering' (UOFC) gives excellent clusters (Gath and Geva, 1989), but does have a fairly long execution time. The difference in clustering between the FCM and FMLE has been shown in section 4.3.3. The images clearly highlight the superiority of FMLE over FCM. The combined algorithm of the UOFC is superior to FMLE as the users' knowledge is not required for effective clustering.

5 IDENTIFYING HYPERDENSITY

Finding the presence of hyperdensity in the brain regions of the images and the development of an algorithm capable of assisting radiologists in their diagnosis of TBM were the ultimate goal of the project. The fact that hyperdense tissue has higher intensity in the images than the surrounding tissue, means that clustering should be able to separate it from normal brain matter and the use of fuzzy clustering allows for the overlap between hyperdense and normal tissue.

5.1 Application of the UOFC algorithm

After the pre-processing of the images discussed in section 4.2 they were ready to be input to the unsupervised optimal clustering algorithm described in section 4.3

The input images to the algorithm consisted of images obtained from 17 TBM positive patients, and from a control group of 9 patients with normal brain CT scans. The patients were all of a similar age (0 -5 years) and all were scanned on the same machine using the standard parameters for brain scans. All images were scanned from film format into digital format. The images were clustered using the UOFC algorithm, and took 15 to 20 minutes per image.

A typical result from a positive TBM patient after clustering resulted in 3 clusters and is illustrated in Figure 5.1

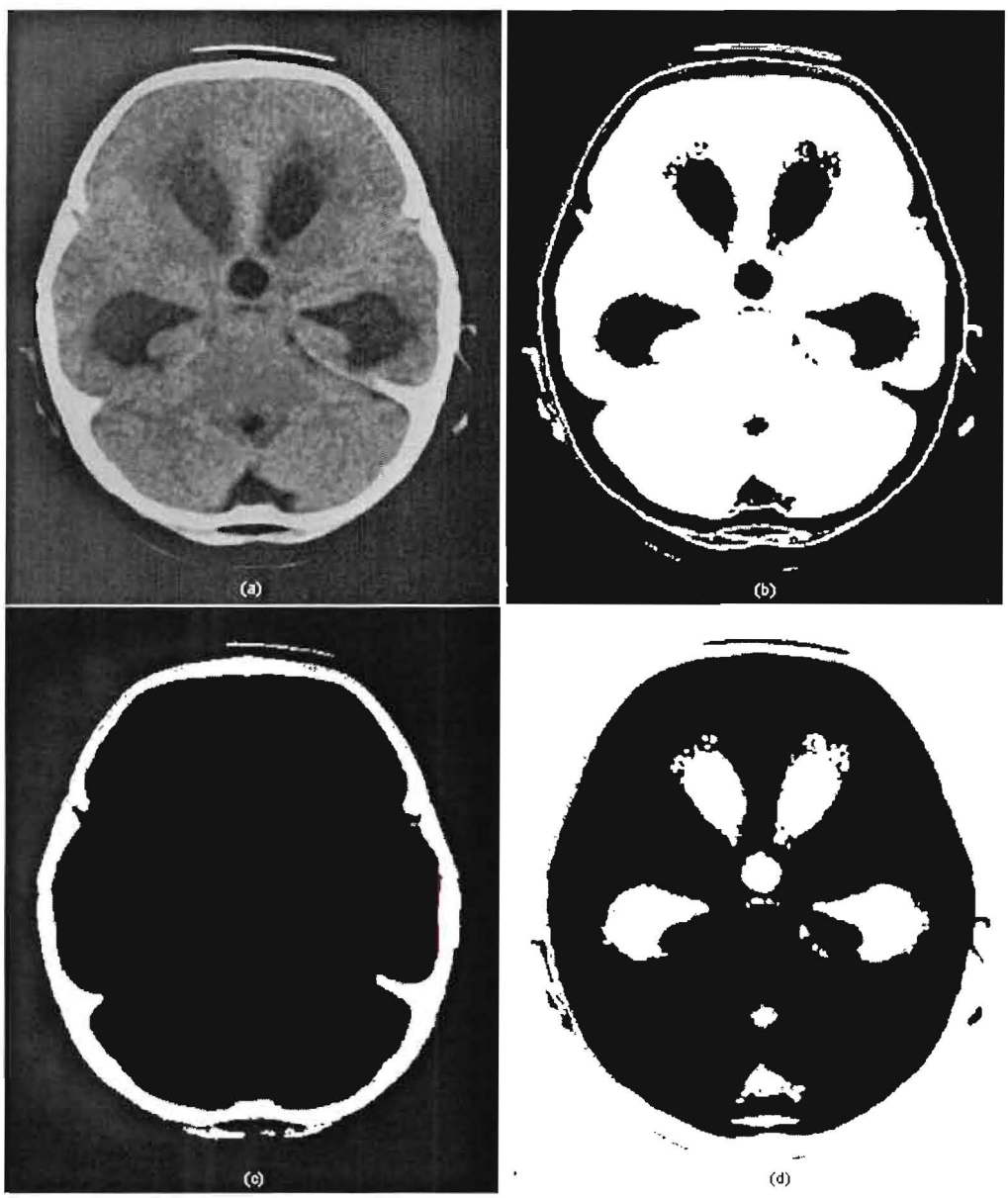

Figure 5.1 : Showing the Original CT image and the resultant clusters after undergoing our unsupervised optimal fuzzy clustering. Image (a) is the original CT image after undergoing pre-processing. Image (b) shows the 'brain' cluster resulting from the UOFC algorithm. Image (c) shows clearly the 'skull' cluster and image (d) shows the 'ventricle' cluster.

The images above show the 3 clusters that our algorithm has selected, namely brain, skull and ventricle. At this stage, the images above do not give any indication as to the presence of TBM. As we are searching for hyperdense tissue in the brain, further clustering of the brain cluster must take place. The other clusters contain very important information, some of which is relevant to TBM and will be discussed later.

In order to do more clustering, we needed to select the pixels identified by the brain cluster from our original image, and then again cluster just that portion representing brain.

The algorithm searched through the clustered image and when it found a pixel associated with the brain cluster, the corresponding pixel in the original was selected. Once every pixel had been examined, what remained were the pixels in the original image representing only the brain.

Figure 5.2 shows the result of removing the skull from the TBM images after undergoing the first segmentation.

Figure 5.2: Image showing only the brain tissue of a TBM positive patient

5.2 Further Segmentation of the brain

The first application of clustering resulted in 3 clusters of which the brain cluster would contain any hyperdensity that might be present. By further segmentation of this region we hoped to extract a cluster consisting of hyperdense tissue and thus highlight the location and shape of the hyperdense tissue in order to assess the likelihood of TBM.

The UOFC algorithm was applied to each of the saved brain segment images from all 17 TBM positive patients. Due to the large number of clusters that resulted, the processing time increased dramatically. It ranged from 1 to 2 hours per image, with most images being clustered into 6 clusters. The number of end clusters differed in each image, hence the large difference in processing time. Once the images were clustered, the clusters were checked visually to see if they included a hyperdense cluster that indicated TBM.

All 17 of the tested images resulted in one cluster that was classified as hyperdense. The number of clusters differed from 4 to 9 clusters, but the common thread was always a cluster containing hyperdense tissue.

Bone is the densest tissue in the body and therefore always shows up in CT scans with high intensity. Once the skull was removed in the first clustering, there still existed a ring of tissue around the brain that was denser than brain tissue. This hyperdensity was due to the uncertainty, and overlapping of the brain and skull tissue. Another reason for this hyperdensity is beam hardening, an artifact inherent in all CT machines; see section 2.5 for more details. These factors may result in a hyperdense cluster being present, but it is important to differentiate this normal hyperdensity from one that indicates diseased tissue. The tentorium of the brain also shows up normally with high intensity and therefore needs to be excluded as a possible abnormality.

The presence of these normal hyperdensities does not indicate TBM. In our case the 17 images that segmented a hyperdense cluster showed further hyperdensity, indicating the possible presence of TBM.

Once the algorithm had segmented out the hyperdense region, we needed to establish that the hyperdensity was indeed abnormal.

The most obvious form of abnormal density in brain CT images of TBM patients, is enhancement in the basal cistern areas, especially around the circle of Willis and in the sylvian fissures (Andronikou *et al*, 2004), usually detected from post contrast scans of TBM patients. Our aim was to do the same detection without the need for contrast enhancement.

When radiologists examine pre-contrast scans for signs of hyperdensity, any tissue other than large blood vessels, that is deemed to be of a higher density than the surrounding tissue is classified as hyperdense. Upon administration of contrast dye, the sign of basal enhancement is not as easy to classify. The contrast dye causes even the smallest blood vessels to enhance dramatically and the radiologist must be careful he/she does not classify a vessel as enhanced tissue. When determining abnormal enhancement there is a strict set of signs that need to observed before conclusions can be made, where as any asymmetrical hyperdense tissue in pre-contrast scans is deemed abnormal.

The hyperdensity, if normal, is usually symmetrical around the vertical axis and so areas that show up as hyperdense on one side of the brain but not the other, usually indicate an abnormality. The 17 hyperdense clusters all showed signs of abnormal hyperdensity with a large degree of asymmetry and a number were hyperdense in the basal cisterns. This leads us to a positive finding of hyperdensity in all our positive TBM patients. Of the 17 TBM positive images chosen in section 4.1, 12 were selected by an expert radiologist and 5 by the author. When comparing these results, no difference was found in the identification of hyperdensity.

The image below is a normal brain CT image after undergoing the UOFC algorithm, showing the cluster of highest density, as evident by the skull outline.

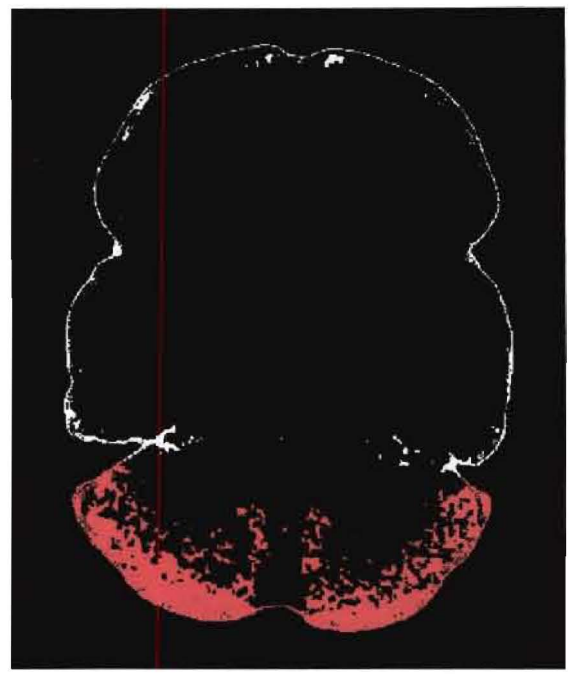

Figure 5.3 : Image showing the highest density cluster from a normal CT scan after undergoing further segmentation by the UOFC algorithm. The red area is the hyperdensity from the tentorium

Figure 5.3 contains most of the common normal hyperdense regions discussed above. Firstly the area coloured in red, is the tentorium and shows up as it should as hyperdense. The perimeter of the brain has shown up as dense, as well as slight beam hardening in certain areas, where the outer perimeter is thicker. The image does not contain hyperdensity that is not connected to the perimeter and which could be classified as abnormal. The full set of Normal results is in Appendix C.

The characteristics of hyperdensity associated with TBM were identified on all 17 images by the author and by an expert in the field of paediatric radiology. The images below highlight a few of the hyperdense regions that were observed. For more detail about the anatomy of the brain see section 2.3.1

Figure 5.4 Show all the brain clusters after the second UOFC clustering. The hyperdense cluster is outlined in red, and is easily identified as the high density tissue, from the outline of the skull. Further details about the hyperdense region follow.

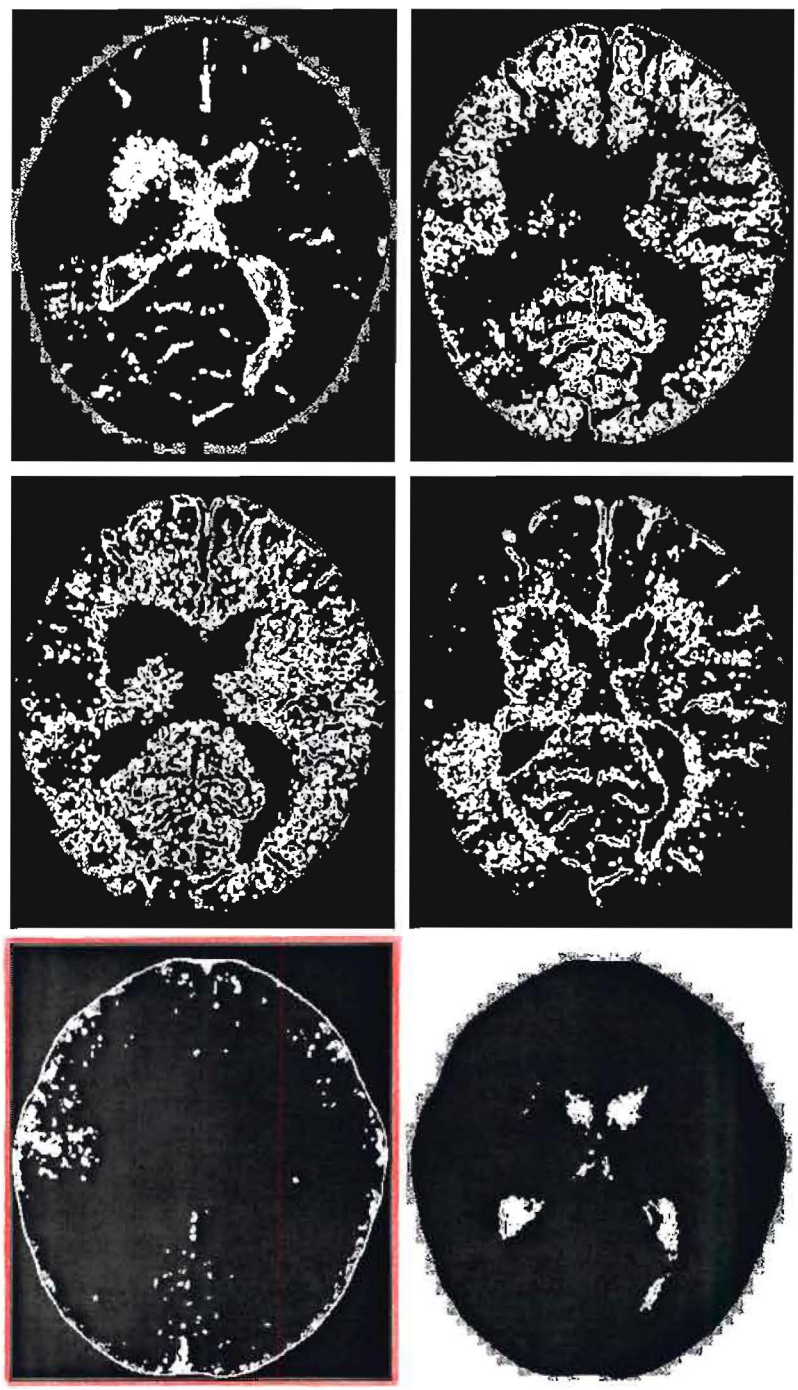

Figure 5.4 : Showing all the clusters that resulted after clustering the brain cluster

The image in Figure 5.5 (a) shows the normal hyperdense characteristics of the outer ring of the brain and mild beam hardening in places where the line appears to be thicker (blue arrow). Near the top of the image it is possible to see a vague area representing the lining covering the brain. This lining in the bottom part of the image is more obvious and is called the tentorium (green arrow). Both these linings are expected to show up as being denser that the surrounding brain tissue.

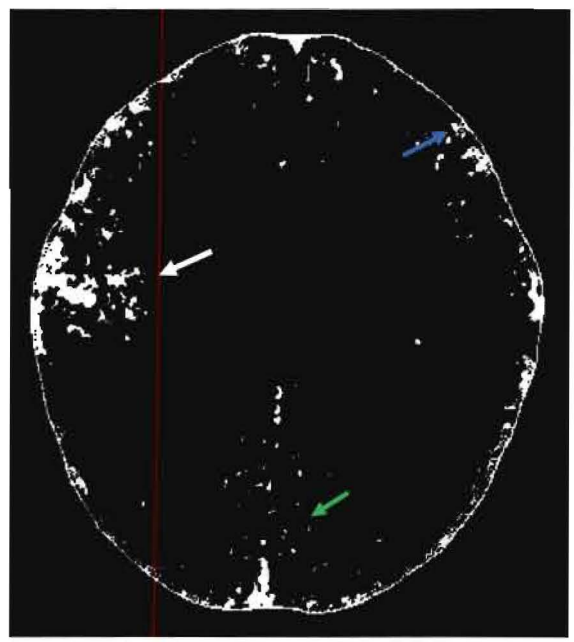

Figure 5.5 (a): Image of the hyperdensity region of a TBM positive patient after further clustering of the brain clusters using UOFC. The arrow shows an area of hyperdensity

The abnormal hyperdensity that is believed to indicate TBM is evident in the left hand area of (a) just to the left of the arrow. This area is clearly enlarged, which it should not be in a normal scan. The abnormality is confirmed by the asymmetry. The same area on the right hand side of the image, shows very little of this same hyperdensity.

Figure 5.5 (b) shows the most common shape of hyperdensity that is associated with TBM, and is seen in and around the basal cisterns.

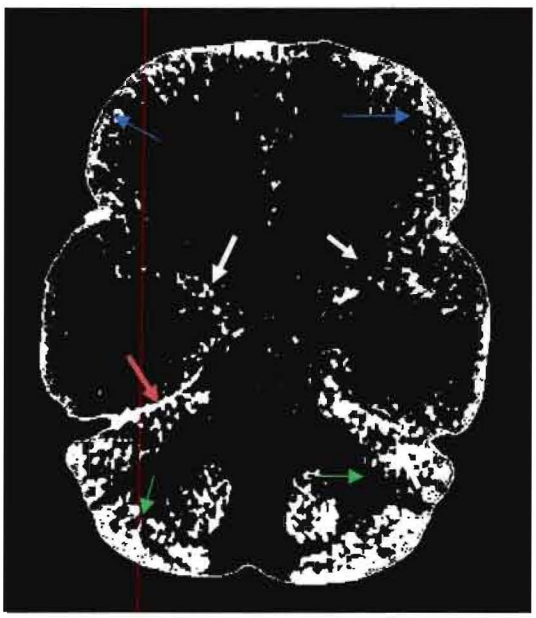

Figure 5.5 (b) : Image of the brain region of a TBM positive patient after further clustering using FMLE. The red arrow indicates a bood vessel, the white arrows indicate hyperdensity, the green arrows show the tentorium and the blue arrows indicate beam hardening

This second example contains more beam hardening than the first – indicated by the blue arrows, and the tentorium is more easily identifiable (green arrows). The red arrow indicates a blood vessel, which has correctly shown up as hyperdense. The area indicated by the white arrows is abnormal, and the distinctive pattern it has formed around the sylvian cistern and fissure will be evident in a number of our results. The dense tissue that the white arrows are pointing to, is spread over a large area, which eliminates the possibility that they are further blood vessels, and are more likely the exudate from the TBM around the blood vessels.

The third example, Figure 5.5 (c) shows the hyperdensity on the opposite side to Figure 5.5 (a). Once again the outer perimeter of the brain has shown up as hyper dense, and once again the linings or membranes of the brain are easily identifiable. There is no mistaking the hyperdensity indicated by the arrow, as it is isolated and distinct

Figure 5.5 (c) : Image of the brain region of a TBM positive patient after further clustering using FMLE

The fourth example, Figure 5.5 (d) has a larger amount of hyperdense tissue than the other examples. The reasons for more dense tissue being present towards the edges could firstly be that the image might show a large amount of beam hardening. The other reason could be that the image contained more noise and therefore more uncertainty. The uncertainty in the image may have caused the noise pixels to be classified as hyperdense tissue. The tentorium is clearly visible with large areas being enhanced (green arrows). The familiar pattern around the sylvian cisterns and fissure is very clear and there are large areas of hyperdensity on both the left and right side.

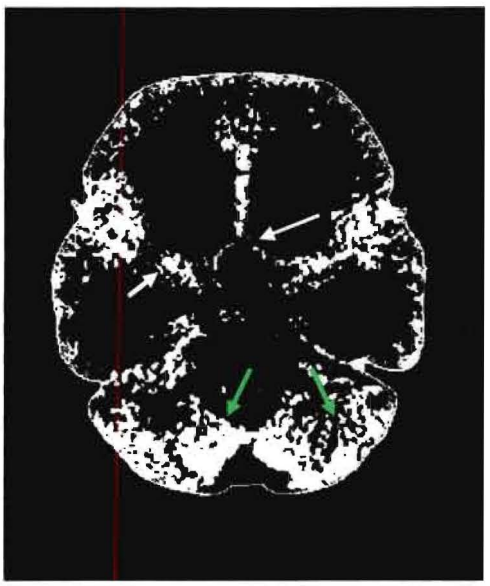

Figure 5.5 (d): Image of the brain region of a TBM positive patient after further clustering using FMLE

The final example used to illustrate hyperdensity (Figure 5.5 (d)), is more subtle than the others, and certainly could have been missed by a radiologist who was checking for hyperdensity.

For comparative purposes we display Figure 5.6 - the original image alongside the hyperdense segment in order to highlight the difficulty of determining hyperdensity by eye.

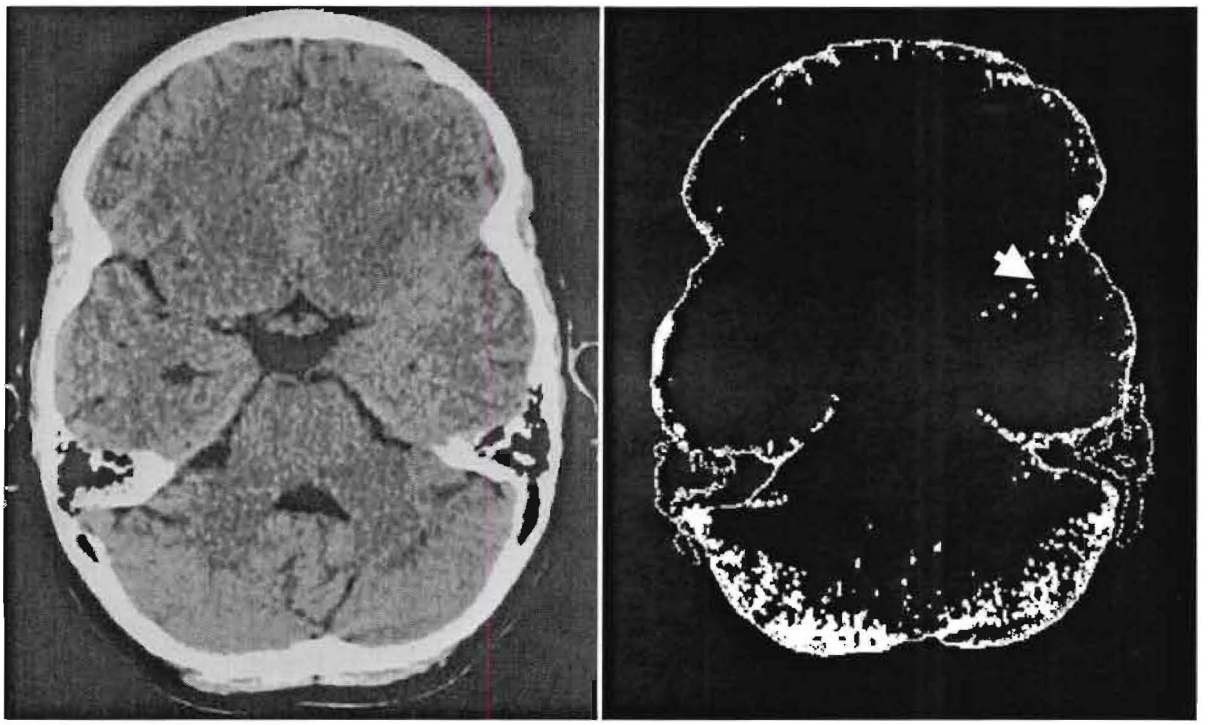

Figure 5.6: Showing the original CT image on the left and the hyperdense cluster on the right after being clustered twice with UOFC.

In the original image the hyperdensity is difficult to visualise. After the clustering it becomes evident that there is hyperdense tissue in the right sylvian fissure – indicated by the arrow, a common place for TBM hyperdensity to show. There is not a large amount of hyperdensity in comparison to our other examples, but it is clearly visible and possibly indicates TBM. The full set of results is available in Appendix B.

6 HYDROCEPHALUS AS A SIGN OF TBM

In Chapter 5, Hyperdensity was identified in all images of TBM positive patients. As a result of the clustering technique presented, a further sign associated with TBM has been identified from the images. This chapter explores the hydrocephalus and its relation to TBM.

6.1 Characteristics of Hydrocephalus

Hydrocephalus is characterised as an enlargement of the ventricles of the brain. In TBM it is possible that the hydrocephalus is caused by the TBM exudate forming adhesions of the basal subarachnoid space. This blockage in the cisterns prevents the CSF from flowing from one ventricle to the next, and so the ventricle that is blocked starts to swell with CSF and is therefore classified as hydrocephalic (Thwaites *et al,* 2000).

The swelling of the ventricles may compress surrounding blood vessels and nerves, causing permanent damage to them. The ventricles must therefore be monitored closely for increased size during treatment of TBM.

From the literature on TBM, hydrocephalus is one of the few signs that is consistently found in TBM patients, especially in children. In a study by Kingsley *et al* (1987) 80% of the children in the study showed the presence of hydrocephalus. In later studies the results were similar, with Thwaites *et al* (2000) finding the presence of hydrocephalus in 87% of the children in the study.

One of the largest studies of CT signs associated with TBM was done by Ozates *et al* (2000) Here 289 patients had their CT scans examined for signs of TBM and here again 80% of the children had hydrocephalus. The study also found that hydrocephalus was commonly present at the time of admission to hospital and tended to become more marked during treatment before it subsided. This highlights the importance of monitoring the hydrocephalus effectively.

Ozates *et al* (2000) went further than just classifying a patient as having hydrocephalus, by separating the findings into mild, moderate and severe. Although it is not specified how these were measured, it was most likely done by eye alone, and therefore would have been subjective.

These studies indicate that hydrocephalus is an important sign associated with TBM, and therefore being able to identify it automatically and more importantly being able calculate its size or area would be beneficial to the radiologist.

6.2 CT measurements of Hydrocephalus

Classification of hydrocephalus usually relies on the radiologists' judgement. When monitoring a patient, it becomes important to have some measurement as comparison by eye may be difficult if the changes are small.

Hydrocephalus is not only caused by TBM but by a number of other sources including trauma. Often shunts need to be placed in these ventricles in order to drain them, and then monitoring the size of the ventricles is even more crucial.

In the past the most common linear measurement was called the Evans ratio (Evans, 1942). It was calculated by measuring the maximum width between the frontal horns of the ventricles and dividng this by the maximum width of the skull. The measurements were taken from the CT image that displayed the maximum span of the ventricles. Countless other linear measurements are used today, but the most accurate way of determining hydrocephalus is by calculating the ventricular volume (Wyper *et al*, 1979).

The ventricular volume is often impractical to measure. MRI is able to do this due to clear distinction between ventricles and brain matter, as well as the large number of slices used in MRI.

In MRI the area of the ventricles in each slice is calculated and the areas are added together in order to calculate the volume. When comparing the evans ratio to this absolute, the correlation is only 0.423 and clearly inadequate in quantifying hydrocephalus (O'Hayon *et al*, 1998).

The method that compares most favourably to the ventricular volume is Ventricle/brain ratio which has a correlation of 0.89 (O'Hayon *et al*, 1998). This ratio is much faster and easier to compute than the total ventricular volume. It is calculated from the ventricular area divided by the total brain area at the level where the lateral ventricles extend the furthest laterally.

In the model shown in Figure 6.1, the ventricular brain ratio is calculated from:

Ventricular brain ratio = Area(■) / Area(■ + ■) ; (11)

This ratio is ideally suited to the clustering technique presented for calculating a measurement of hydrocephalus. The combination could be applied to all types of hydrocephalus, not just those related to TBM.

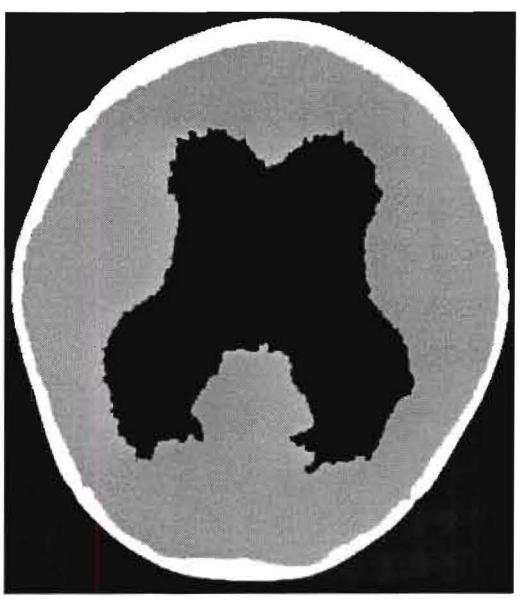

Figure 6.1 : Image showing a model of the brain with the skull, ventricle and brain matter areas in different colours.

6.3 Method of Hydrocephalus measurement

The results of the UOFC algorithm, prepares the data for use in calculating the ventricular brain ratio. The brain area and the ventricle areas have been segmented out of the original, and can be used in calculating the ratio.

The CT image in which the ventricles extend furthest laterally is used in the calculation of the ratio. These images were segmented using the UOFC algorithm for 17 TBM patients.

Matlab has a built in function that allows for labelling all connected areas in an image, which is called *bwlabeln*. The labelling method was applied to the ventricle clusters. Once this was complete the ventricle area was calculated by using another Matlab function, which counted the number of pixels in the labelled region.

The same procedure was repeated for the brain cluster and thus gave us the brain area. The ventricles weren't included in the brain area as they did not belong to that segment. The ventricle area was therefore added to the brain area, in order to obtain the total brain area.

The ventricular brain ratio (VBR) was then found by dividing the ventricle area by the total brain area as indicated in equation (11).

Synek *et al* (1976) first documented the use of the VBR in distinguishing patients with normal and abnormal ventricular size, corresponding to either atrophy or hydrocephalus. Atrophy would not commonly be associated with this patient group due to the young age of the patients, therefore abnormal VBR in this case would be in relation to hydrocephalus.

VBR was converted to a percentage for ease of comparison, and it was found that the normal patients had a ventricle to brain percentage of approximately 5% but it ranged from 1 to 9%. The abnormal case of hydrocephalus was always greater than 10% (Synek *et al,* 1976).

From the 17 positive TBM patients that underwent the ratio measurements, 12 had ratios that suggested hydrocephalus. These findings indicate the prevelence of hydrocephalus in the positive TBM patients to be 71%. This figure corresponds with the literature on TBM related hydrocephalus.

Figure 6.2 shows the large variation in ventricle area compared to brain area for our TBM patients. The black line at the 9% mark indicates the upper threshold of the normal VBR, and all columns that extend above it, are indicators of hydrocephalus. The upper threshold of 9% is taken from the literature (Synek *et al,* 1976).

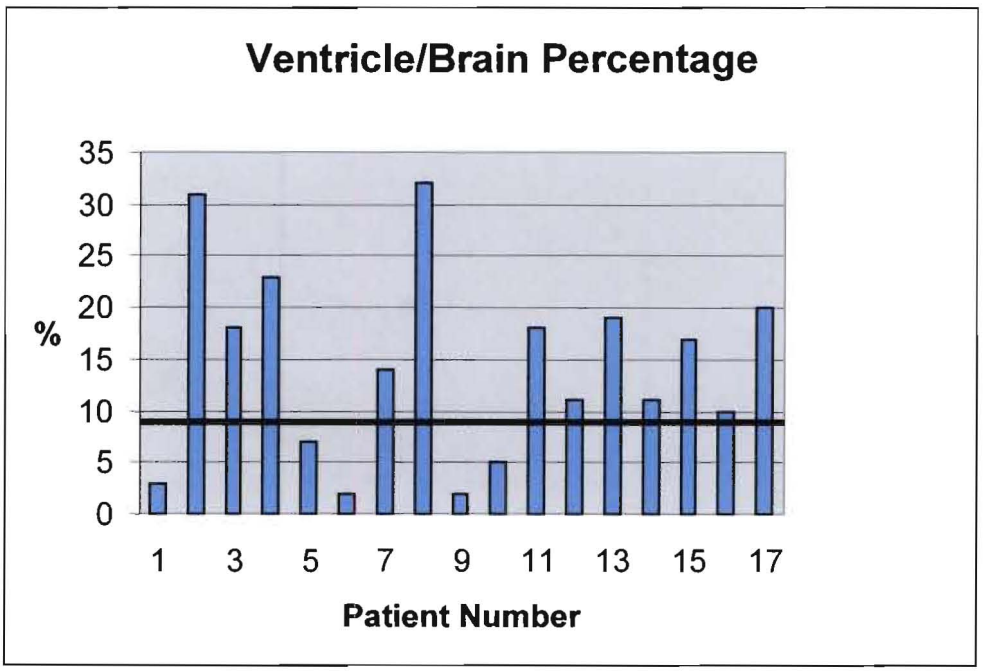

Figure 6.2 : Showing a graph of VBR as a percentage for all 17 positive TBM patients.

The control data unfortunately did not contain a full set of CT slices and only two of the normal patients had suitable images for calculation of the brain/ventricular ratio. The 2 images had values of 1.4% and 2.1% which were well below the abnormal percentage of 9%.

6.3.1 Errors in Calculation

The errors in hydrocephalus calculation include those that were inherent in the segmentation using UOFC. Misclassification is the most obvious of the errors and therefore could result in inaccurate area calculation. The effect of the misclassifications are difficult to quantify, but are thought to have very little influence on the overall areas calculated.

7 Conclusions

The results of our study have supported our original hypothesis that hyperdensity is present in the CT brain scans of TBM patients. Hyperdense areas have been segmented from CT scans and a further TBM sign, hydrocephalus, has been measured.

7.1 CT number reconstruction

Reconstructing the CT numbers from hard copy CT films was the first objective of this project. This was done in order to prove Dr Andronikous' theory of hyperdensity being present in pre-contrast films of TBM positive patients (Andronikou *et al*, 2004).

We successfully reconstructed these CT numbers with some limitations, and were able to determine the density of all the pixels in each image. Dr Andronikous' theory was then proved by finding pixels that had abnormally high density in the brain region of TBM patients.

Hyperdensity has appeared in very few papers in the literature to date, and is possibly a new, unique sign associated with TBM. The difficulty in determining hyperdensity is the most likely cause of the sign not currently being included in TBM diagnosis. Even experienced radiologist who are specialists in TBM have difficulty detecting hyperdensity, and therefore it is mostly noted after the administration of a contrast dye, which enhances the areas with abnormal density.

By using pattern recognition we have managed to extract this hyperdensity without the need for contrast enhancement, therefore reducing the risk to the patient.

7.2 Hyperdensity Segmentation

Pattern recognition is very important in identifying objects that may be difficult to identify using the human eye. The limitation of the human eye of being able to differentiate no more than 16 grey values at a time often means than subtle contrast differences may be missed. By using pattern recognition, in particular – clustering, these small differences can be highlighted for the user.

We chose to use clustering in this project after careful consideration of the prior literature. New techniques are being developed daily, but all have a compromise between execution time and the quality of results. Due to the advent of MRI and its superior capability over CT for soft tissue imaging, very little research into CT segmentation has been done in recent years. In developing countries like South Africa the cost of MRI is too high for most public hospitals and CT scanners are the method of choice.

Fuzzy clustering was chosen as our initial segmentation method. Fuzzy logic helped approximate the uncertainty that is inherent in CT images, and ultimately provided better clustering of the images. The superiority of fuzzy c-means clustering was demonstrated in section 4.3.1 where it was compared to simple k-means clustering. The choice of the fuzzy maximum likelihood estimation algorithm was supported by previous use in brain clustering by Cosic *et al* (1996). Pre-processing in the form of contrast stretching, enhanced the contrast in our images before they were clustered, and also contributed to better results and faster execution time.

The final algorithm was unsupervised and did not rely on prior knowledge of the images. The results of the segmentation clearly showed the initial optimal number of clusters to be 3 – those being skull, ventricle and brain. Upon further segmentation of brain region using UOFC, a hyperdense region resulted in all of our positive TBM patients.

The hyperdense region showed all the characteristics of abnormal hyperdensity discussed in section 5, and to verify these results, the same process was repeated on a number of normal CT

scans. The normals lacked the abnormal hyperdensity, leading us to conclude a 100% finding of hyperdensity in TBM positive patients, concurring with the radiologists' findings (Andronikou *et al,* 2004).

7.3 Hydrocephalus

As a result of the UOFC algorithm used to cluster the images, it was possible to detect another sign associated with TBM. Hydrocephalus is strongly supported in the literature as a sign commonly associated with TBM. The increase in ventricle size is important when monitoring the progression of the disease, and the ability to calculate the size of ventricles would be beneficial to the radiologist.

The use of UOFC algorithm allowed us to segment the ventricle region from the brain scans. From this we were able to calculate a brain/ventricular ratio, which was able to determine the presence of hydrocephalus in the images. 71% of the TBM patients had ratios that indicated hydrocephalus.

The overall findings of hyperdensity and hydrocephalus have accomplished the aims of this project and show how a program such as the one discussed would be beneficial not only to the radiologist but to the overall care of the patient.

7.4 Presentation to Radiologist

The way the results are interpreted is important in making the correct diagnosis of TBM. Therefore hiding the working of the program and yet showing all pertinent results to the radiologist using the program were necessary.

The use of the unsupervised algorithm meant that the radiologist needed only to specify the image to be checked for TBM, and start the program running. After the first set of clustering the radiologist would identify the brain cluster for further segmentation. Once this was complete a number of images would be output to the screen showing the resultant clusters.
The hyperdense cluster would be identified by the outer ring of brain tissue and the obvious signs of beam hardening which must be associated with higher density tissue.

The radiologist can then examine the high density cluster for signs of hyperdensity and draw conclusions from these.

When checking for hydrocephalus the radiologist would need to select the ventricle cluster after the first segmentation. When the program is run the radiologist would then use the mouse to identify the ventricles and brain as prompted, and the program would output the ventricular/brain ratio as a %, as well as the normal value for comparison.

With both these findings the radiologist would be able to specify a diagnosis of TBM with more authority.

7.5 Recommendations

The project has accomplished its goals but in the process has uncovered more areas of research that should be explored. The use of the UOFC algorithm has proved successful, but a number of possibilities remain for improving its accuracy. The spatial aspects of images are not taken into account by the algorithm and therein lies an area of improvement (The influence of the surrounding pixels aren't taken into account). By comparing the pixels surrounding the one of interest, it may be possible to determine whether the pixel has been affected by noise. Eg: if all the surrounding pixels were white but the pixel of interest was black, it was probably corrupted by noise.

Many new algorithms that combine fuzzy clustering and neural networks are being used on MRI images in order to segment them, and similar techniques could be applied to CT images.

Hyperdensity was a subtle and difficult sign to detect visually. Another area where the clustering would be valuable to detect subtle differences in intensity is oncology. The detection of a brain tumor would be easily accomplished using this algorithm, and tracking of the growth of a tumor would also be possible during treatment. It may also have potential in determining the type of cancer, by clustering certain characteristics that may define the type of cancer.

The UOFC algorithm has not been used on MRI images and could prove to be very effective in segmenting them.

Ultimately the algorithm may be beneficial to any segmentation problem where uncertainty exists and where prior knowledge about the image is unknown. The unsupervised qualities mean that the algorithm does not rely on user knowledge and would be easily implemented without expert assistance.

The segmentation algorithm presented should be validated further by applying it to all the images used in the Andronikou *et al* (2004) study. The remaining scans should be segmented for hyperdensity as well as ventricular volume measurement, i.e the TBM positive scans with no pre-contrast density and all TBM negative scans should be segmented. In this manner the sensitivity and specificity of hyperdensity and hydrocephalus using the UOFC algorithm could be compared to radiologists' inspection of CT numbers (in the case of hyperdensity) and visual inspection (in the case of hydrocephalus).

8 Appendices

A Results of Hyperdensity Validation

The Table below contains all the pixels that were selected to be verified.

Calc CT	Actual CT
7	10
65	55
34	28
29	29
15	20
23	21
28	26
59	51
29	31
6	9
62	50
44	40
6	10
26	27
36	37
31	31
32	34
29	26
40	40
8	10
30	31
33	33
31	34
36	36
39	35
26	26
5	8
40	37
30	28
25	29
23	22
21	22
41	38
30	34
26	25
65	61

65	53
30	30
65	53
53	52
15	16
53	52
Correlation = 0.98177	

B Hyperdensity Results in TBM positive patients

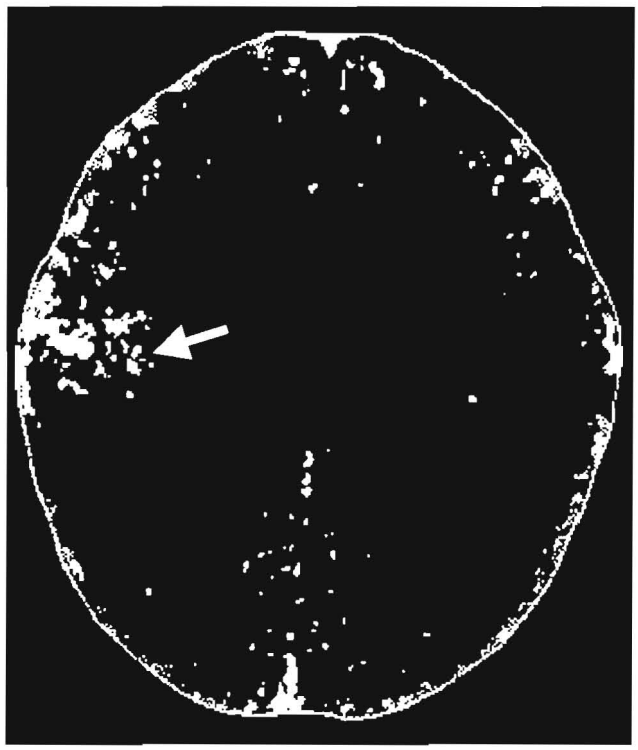

The arrow indicates the area of hyperdensity. The tentorium near the bottom of the image is also seen as hyperdense, but is normal.

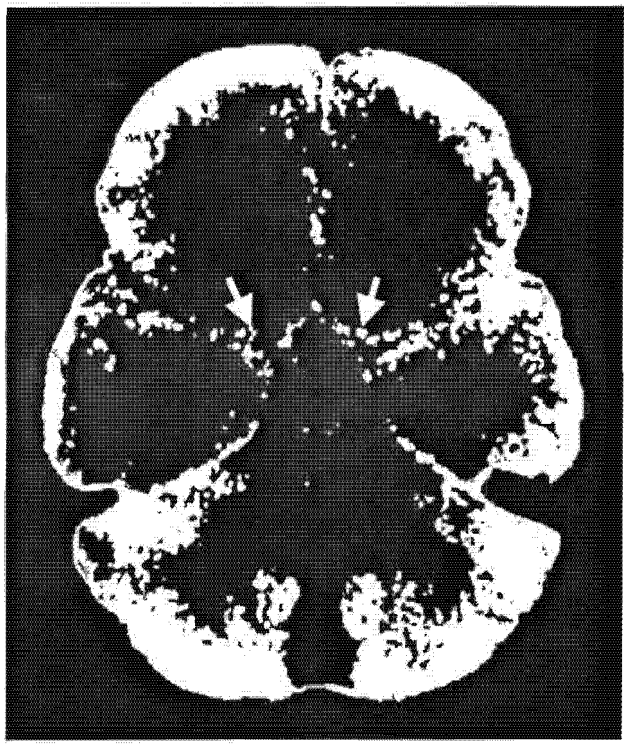

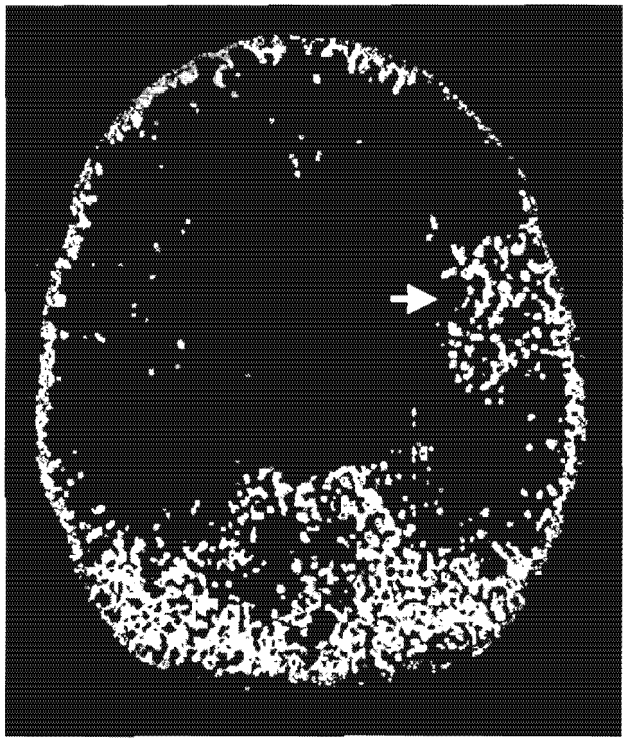

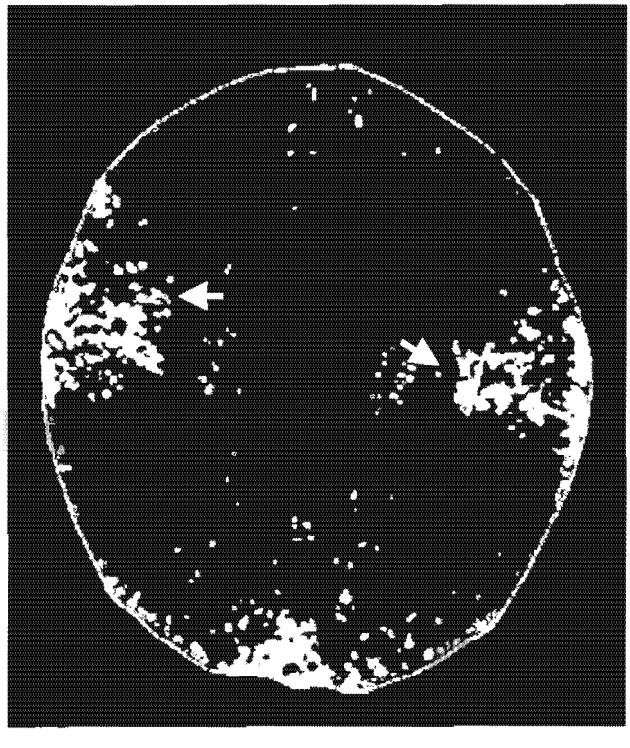

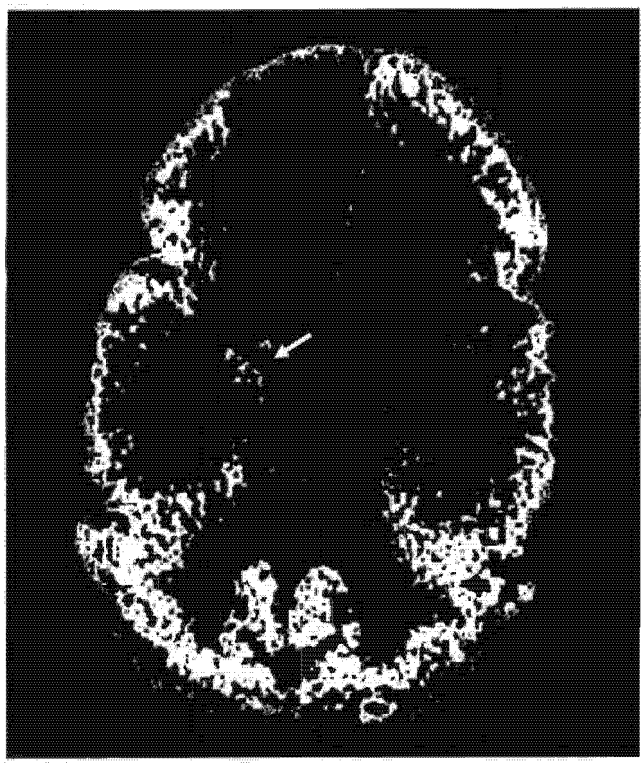

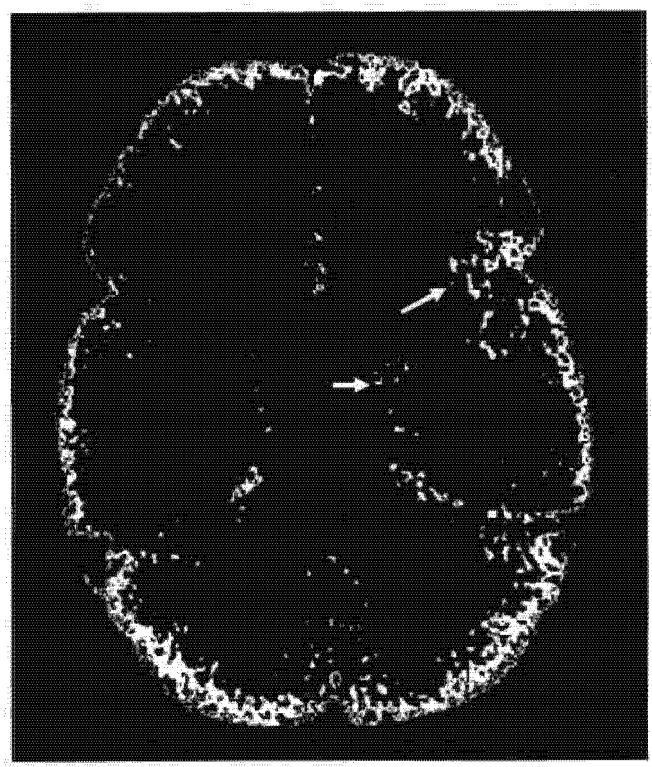

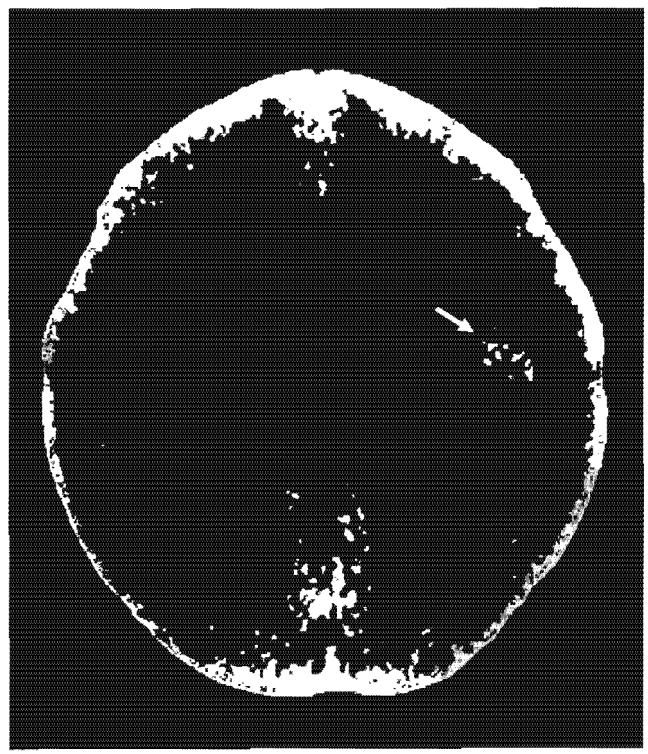

C Normal CT results

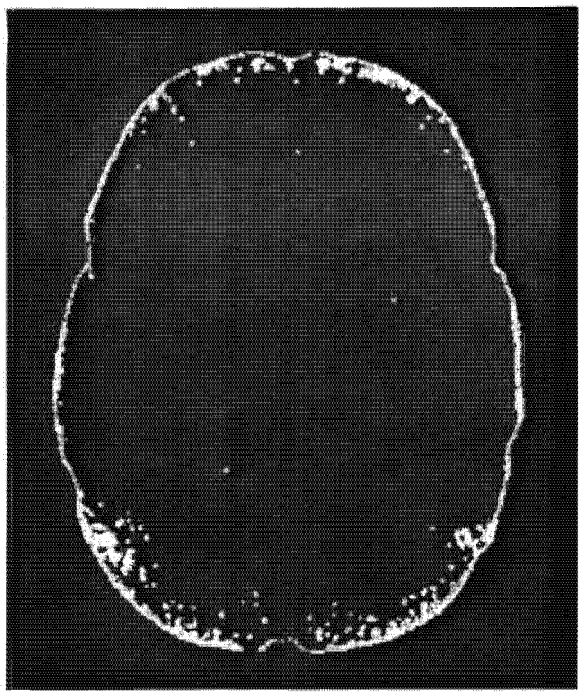

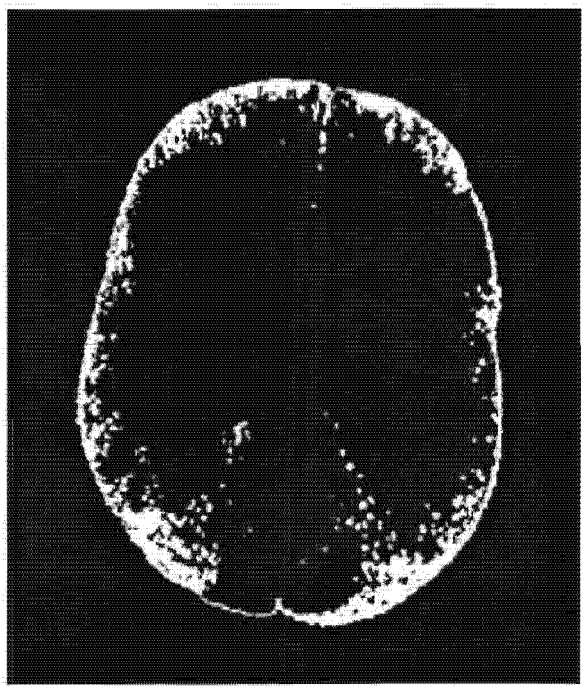

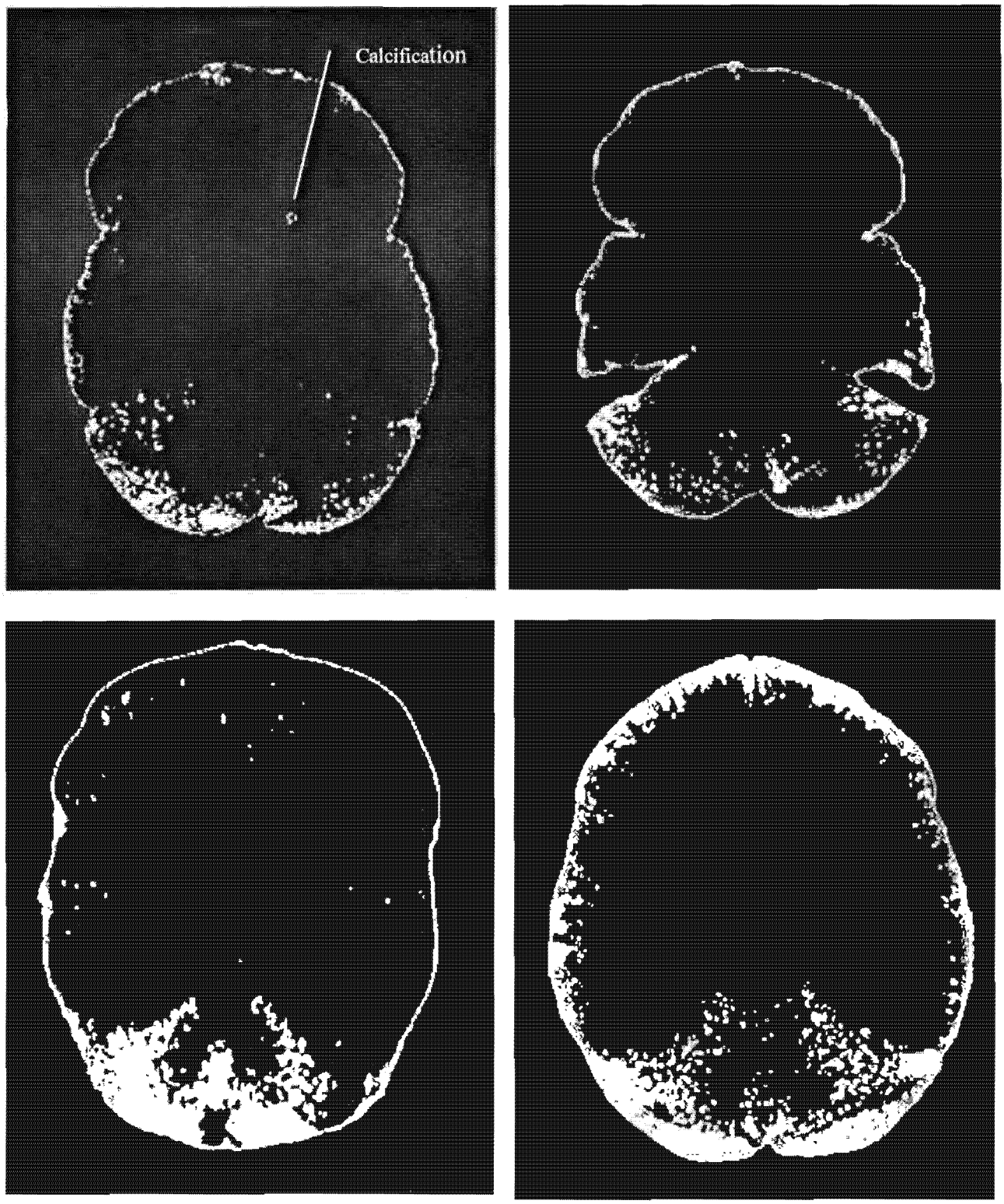
Calcification

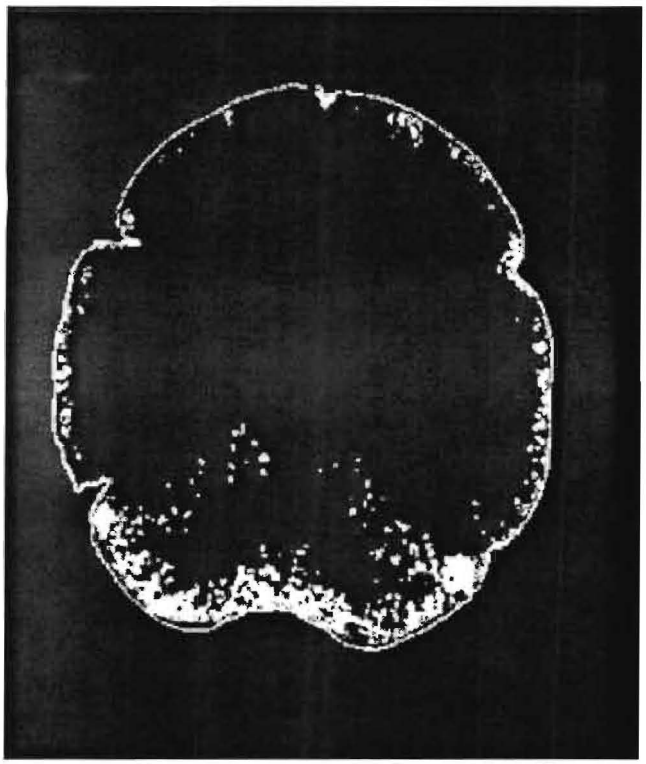

D Program Files

The programs can be found on the CD enclosed with this project.

The FCM.m file is the code for the simple fuzzy c-means algorithm and will cluster an image using the FCM algorithm into a number of clusters specified by the user.

The UOFC1.m is the program that is run first when segmenting an image using UOFC clustering. Only the name of the image needs to be entered by the user and the program computes the clustering.

After UOFC1.m is run, GETBRAIN.m must be run in order to generate the brain cluster to be fed into UOFC2.m.

The final UOFC2.m is then run in order to cluster the brain image into a number of clusters, one of which contains hyperdensity in the case of a TBM positive patient.

9 REFERENCES

Andronikou S, Smith B, Hatherhill M, Douis H, Wilmshurst J (2004) Definitive Neuroradiological Diagnostic Features of Tuberculous Meningitis in Children. *Pediatric Radiology* 34: 876-885

Banerjee S, Mukherjee D, Majumdar D (1999) Fuzzy C-Means Approach to Tissue Classification in Multimodal Medical Imaging. *Information Sciences* 115: 261- 279

Bezdek J (1981) Pattern Recognition with Fuzzy Objective Function Algorithms. Plenum Press, New York

Bezdek J, Pal S (1992) Fuzzy Models for Pattern Recognition. IEEE Press, Piscataway New York

Bishburg E, Sunderarm G, Reichman LB, Kapila R (1986) Central Nervous System Tuberculosis with Acquired Immunodeficiency Syndrome and its Related Complex. *Ann Internal Medicine* 105:210-213

Brandt M, Bohan T, Kramer L, Fletcher J (1994) Estimation of CSF, White and Gray Matter Volumes in Hydrocephalic Children Using Fuzzy Clustering of MR Images. *Computerized Medical Imaging and Graphics* 18:25-34

Bushburg J, Seibert J, Leidholdt E, Boone J (1994) The Essential Physics of Medical Imaging. Williams and Wikins, Baltimore, Maryland, USA

Coleman GB, Andrews HC (1979) Image segmentation by clustering. *Proc IEEE* 5:773-85

Cosic D, Loncaric S (1996) New Methods for Cluster Selection in Unsupervised Fuzzy Clustering. *Proceedings of the 41st Annual Conference of koREMA'96* 4:1-3, Opatijia, Croatia

Dowsett D, Kenny P, Johnston R (1998) The Physics of Diagnostic Imaging. Chapman & Hall publishing, London

Evans WA (1942) An encephalographic ratio for estimating ventricular enlargement and cerebral atrophy. *Archives of Neurology and Psychiatry* 47: 931-937

Fike JR, Cann CE, Berninger WH (1982) Quantitative Evaluation of the Canine Brain using Computed Tomography. *Journal of Computer Assisted Tomography* 6:2 325-33

Gath I, Geva A (1989) Unsupervised Optimal Fuzzy Clustering. *IEEE Transactions on Pattern Analysis and Machine Intelligence* 11(7): 773-781

Gustafson D, Kessel W (1979) Fuzzy Clustering with a Fuzzy Covariance Matrix *Proceedings of IEEE CDC,* San Diego, CA, 776-766

Guy C, Ffytche D (2000) An Introduction to the Principles of Medical Imaging Imperial College Press, Covent Garden, London

Haaga J, Lanzieri C, Gilkeson R (2003) CT and MR Imaging of the Whole Body, Mosby Publishing. 11830 Westline Industrial Drive, St Louis, Missouri

Hall L, Bensaid A, Clarke L, Velthuizen R, Silbger M, Bezdek C (1992) A Comparison of Neural Network and Fuzzy Clustering Techniques in Segmenting Magnetic Resonance Images of the Brain. *IEEE Transactions on neural networks,* 3:5 672-681

Hedlund LW, Vock P, Effman EL (1983) Computed Tomography of the Lung – Densitometric Studies *Radiologic Clinics of North America* 21:4 775-87

Kingsley DPE, Hendrickse WA, Kendall BE, Swash M, Singh V (1987) Tuberculous Meningitis: Role of CT in Management and Prognosis. *Journal of Neurology Neurosurgery, and Psychiatry* 50: 30-36

Loncaric S, Dhawan A, Cosic D, Kovacevic D, Broderick J, Brott T (1999) Quantitative Intracerebral Brain Hemorrhage Analysis. *Proceedings of SPIE Medical Imaging* 3661: 886 894

Loncaric S, Cosic D, Dhawan A (1996) Hierarchical Segmentation of CT Head Images *Proceedings of the 18th Annual Conference of IEEE EMBS*

Kumar R, Singh S, Kohli N (1999) A Diagnostic Rule for Tuberculous Meningitis *Arch Dis Child* 81:221-224

Marshall WH, Easter W, Zatz LM (1977) Analysis of the Dense Lesion on Computed Tomography with Dual KVp scans. *Radiology* 124:87-89

O'Hayan B, Drake J, Ossip M, Tuli S, Clarke M (1998) Frontal and Occipital Horn Ratio: A Linear Estimate of Ventricular Size for Multiple Imaging Modalities in Pediatric Hydrocephalus. *Pediatric Neurosurgery* 29: 245- 249

Nevin , Mohamed A, Ahmed M, Farag A (1999) Modified Fuzzy C-Mean in Medical Image Segmentation. *IEEE Proceedings International Conference on Acoustics, Speech, and Signal Processing* 6: 3429 - 3432

NIST/SEMATECH e-Handbook of Statistical Methods, http://www.itl.nist.gov/div898/handbook/, last accessed 25 October 2004.

Ozates M, Kermalog S, Gurkan F, Ozkan U, Hosoglu S, Simsek MM (2000) CT of the Brain in Tuberculous Meningitis *Acta Radiologica* 41: 13-17

Phelps ME, Hoffman EJ, Ter-Pogossian MM (1975) Attenuation Coefficients of Various Body Tissues, Fluids and Lesions at Photon Energies of 18 to 136 keV. *Radiology* 117: 573-83

Rajapakse J, Giedd J, Rapoport J (1997) Statistical Approach to Segmenation of Single-Channel Cerebral MR. *IEEE Transactions on Medical Imaging,* 16:2

Rao SP, ALfidi RJ (1981) The Environmental Density Artifact: A Beam Hardening Effect in Computed Tomography. *Radiology* 141:223-27

South African Department of Health Website – Tuberculosis Statistics 2001 http://www.doh.gov.za/tb, last accessed on 10 November 2004

South African National Tuberculosis Association, http://www.santa.org.za, last accessed on 10 November 2004.

Stimac (1992) Introduction to Diagnostic Imaging, Saunders Publishing, Philadelphia

Synek V, Reuben J (1976) The Ventricular-Brain Ratio Using Planimetric Measurements of EMI Scans. *British Journal of Radiology* 49: 233-237

Thwaites G, Chau T, Mai N, Drobniewski F, McAdam K, Farrar J (2000) Neurological Aspects of Tropical Disease: Tuberculous Meningitis. *Journal Neurological, Neurosurgery and Psychiatry* 68:289-299

Webb S (1992) The Physics of Medical Imaging, Institute of Physics Publishing. Bristol & Philadelphia. IOP Publishing Ltd 1988 Techno House, Redcliffe Way, Bristol

Weyer K, Fourie PB (1989) Die Epidemiologie van Tuberkulose in Suider-Afrika. CME 7: 239-247

Wyper Dj, Pickard JD, Matheson M (1979) Accuracy of ventricular volume estimation. *Journal of Neurology, Neurosurgery and Psychiatry* 42: 345-350

Zadeh L (1965) Fuzzy Sets. *Information and Control* 8:338-353

Zatz LN, Alvarez RE (1977) An Inaccuracy in Computed Tomography: The Energy Dependence of CT Values. *Radiology* 124:91-97

Zerhouni EA, Spivey JF, Morgan RH, Leo FP, Sttik FP, Siegelman SS (1982) Factors Influencing Quantitative CT Measurements of Solitary Pulmonary Nodules. *Journal of Computer Assisted Tomography* 6(6): 1075-1087